Applied Thermal Engineering 256 (2024) 124191

Contents lists available at ScienceDirect

Applied Thermal Engineering

journal homepage: www.elsevier.com/locate/apthermeng

Research Paper

Modeling polydispersed droplets in non-equilibrium condensing CO_2 flows through turbine cascades using moment-based methods for efficient energy utilization

Giuseppe Petruccelli [a,b,*], Amir Momeni Dolatabadi [a], Aki Grönman [a], Teemu Turunen-Saaresti [a], Alberto Guardone [b]

[a] Lappeenranta-Lahti University of Technology LUT, School of Energy Systems, 53851 Lappeenranta, Finland
[b] Politecnico di Milano, Department of Aerospace Science and Technology, 20156 Milano, Italy

ARTICLE INFO

Keywords:
Turbine cascades
Carbon dioxide
Non-equilibrium
Two-phase flow
Supercritical
Polydispersed droplets

ABSTRACT

The efficiency of a power cycle is significantly influenced by the condensation process and the size distribution of the droplets, as these factors directly affect heat transfer rates and overall energy conversion efficiency. Accurate numerical modeling of thermodynamic non-equilibrium condensation is crucial for predicting droplet nucleation and growth in carbon dioxide flows. This study applies moment-based polydispersed droplet models, such as the quadrature method of moments, to account for the droplet size spectrum. Additionally, discrete methods based on a predefined shape of the polydispersed droplet size spectrum are utilized and evaluated to reduce numerical complexity. Our results demonstrate that polydispersed models provide higher accuracy compared to monodispersed models when simulating steam and supercritical carbon dioxide flows in converging–diverging nozzles. In turbine cascades, the choice of model significantly influences the predicted mean droplet size and efficiency. Isentropic efficiency evaluations reveal higher values for carbon dioxide compared to steam, with efficiencies of 94.6–95.8% versus 91.8–92.9% for wet cases and 96.5–97.2% versus 95.8–96.5% for dry cases. Notably, spontaneous droplet nucleation slightly affects the efficiency of the blade cascade in carbon dioxide flows, whereas steam flows experience efficiency reductions between 3.58% and 4.01%. This work advances the understanding of droplet condensation processes in turbine cascades, highlighting the superior performance of polydispersed models and providing quantitative insights into their impact on efficiency.

1. Introduction

Superheated dry flows undergoing adiabatic expansion reach a supersaturated state before the nucleation and growth of liquid droplets, whose temperature differs from that of the vapor flow. This phenomenon can occur under various thermodynamic conditions and flow regimes, impacting the performance of components, particularly those involving high-speed wet flows. Supercritical carbon dioxide (sCO_2) has garnered significant attention as a promising fluid for various industrial applications, including power generation from fossil [1], solar [2], or nuclear [3] heat sources, as well as waste heat recovery [4] and refrigeration [5]. sCO_2 exhibits unique thermodynamic properties that offer advantages in efficiency, compactness, and environmental sustainability compared to conventional working fluids. Many sCO_2 applications operate in transcritical conditions, and accurate modeling of the near-critical phase transition, which is linked to the highly nonlinear behavior of thermodynamic properties, poses challenges for numerical simulations. sCO_2 compressors are operated very close to the critical point to optimize cycle efficiency for power generation [6]. The rapid expansion occurring on the suction side of the compressor impeller blade may lead to the sudden formation of liquid droplets, potentially affecting compressor efficiency [7]. In the context of Carbon Capture and Storage (CCS), supersonic separators are components designed to expand CO_2 mixtures to supersonic speeds, leading to the formation and separation of liquid droplets from the primary flow [8]. This is achieved by generating a swirl flow, for instance, with blades [9] or a cyclone [10]. Accurate modeling of thermodynamic non-equilibrium condensation is imperative for achieving high-fidelity numerical tools for designing these components operating with sCO_2.

Non-equilibrium condensation significantly impacts the efficiency and performance of various energy systems. In compressed air energy

* Corresponding author at: Lappeenranta-Lahti University of Technology LUT, School of Energy Systems, 53851 Lappeenranta, Finland.
E-mail address: giuseppe.petruccelli@lut.fi (G. Petruccelli).

https://doi.org/10.1016/j.applthermaleng.2024.124191
Received 11 April 2024; Received in revised form 11 July 2024; Accepted 14 August 2024
Available online 15 August 2024

Nomenclature

a_i, b_i	elements of the Jacobi matrix
a, b	integration range
b_x	axial chord [m]
c_p	isobaric specific heat [J/(kg K)]
C_V	coefficient of variation
f_η	droplet number density function [1/m]
$\widehat{f}_\eta$	droplet number density function scaled to unity
h	specific enthalpy [J/kg]
K	turbulence kinetic energy [J/kg]
Kn	Knudsen number
k	thermal conductivity [W/(m K)]
k_B	Boltzmann constant [J/K]
J	nucleation rate [1/(m^3 s)]
J_3	Jacobi matrix
j	moment index
M_m	molecular mass [kg]
m	scaling factor
mfp	mean free path [m]
n	number of radii/weights
N	number of subdivisions for numerical integration
N_{exp}	number of measured locations
p	pressure [Pa]
Pr	Prandtl number
$\dot{p}$	expansion rate
Q_{conv}	convective heat transfer source term [J/(m^3 s)]
R	gas constant [J/(kg K)]
r_{10}	mean radius [m]
r_{32}	Sauter radius [m]
r_i	discrete radii [m]
r_{log}	lognormal median [m]
$\dot{r}$	droplet growth rate [m/s]
S	supersaturation ratio
S_q	source term in a transport equation for scalar q
s	specific entropy [J/(kg K)]
T	temperature [K]
t	time [s]
$\boldsymbol{u}$	velocity vector [m/s]
u,v	velocity components [m/s]
w_i	discrete weights [1/kg]
$\widehat{w}_i$	normalized weights
x,y	cartesian coordinates [m]
Y	pressure loss coefficient
z	compressibility factor

Greek letters

α	volume fraction
Γ	diffusion coefficient [kg/(m s)]
η	droplet density [1/m^3]
η_{is}	isentropic efficiency
λ	eigenvalues
μ_j	moments [m^j/kg]
μ	dynamic viscosity [Pa s]
μ_T	dynamic eddy viscosity [Pa s]
ρ	density [kg/m^3]
σ	planar surface tension [N/m]
σ_{gauss}	normal standard deviation [m]
σ_{log}	lognormal shape parameter
$\overline{\overline{\tau}}$	stress tensor [N/m^2]
$\overline{\overline{\tau_T}}$	Reynolds stress tensor [N/m^2]
$\boldsymbol{v}$	eigenvectors
ϕ	generic quantity
χ	normalization coefficient

Subscripts and superscripts

c	critical point
eff	effective
exp	experiments
fg	latent heat
gauss	normal distribution
growth	droplet growth
in	inlet section
is	isentropic process
l	liquid
log	lognormal distribution
m	mixture
nuc	droplet nucleation
out	outlet section
s	saturation
v	vapor
0	total quantity
*	critical quantity

Acronyms

CAES	Compressed Air Energy Storage
CCS	Carbon Capture and Storage
CFD	Computational Fluid Dynamics
CNT	Classical Nucleation Theory
HP	High-Pressure
LP	Low-Pressure
NDF	Droplet Number Density Function
QMOM	Quadrature Method of Moments
MOM	Method of Moments
RANS	Reynolds-Averaged Naver-Stokes
RMSPD	Root Mean Square Percentage Difference
sCO_2	Supercritical Carbon Dioxide
UDF	User-Defined Function
UDRGM	User-Defined Real Gas Model
UDS	User-Defined Scalar

storage (CAES), air is compressed and stored in large underground reservoirs, then released to generate electricity during peak demand periods. The moisture in the airflow affects blade erosion and compressor efficiency [11], influenced by heterogeneous condensation due to foreign particles [12]. Similarly, the design and operation of supersonic ejectors, widely used to enhance refrigeration performance, are heavily dependent on the formation and interaction of liquid droplets with the primary flow [13,14]. Supersonic ejectors utilize high-speed jets to entrain and compress a secondary fluid, creating a vacuum effect. The presence of liquid droplets can alter the shock wave structure within the ejector, leading to variations in mixing efficiency and pressure recovery.

In high-speed condensing flows, a temperature difference between the vapor and liquid phases naturally occurs in the metastable region during the development of liquid droplets. Thermodynamic non-equilibrium condensation models account for this phenomenon and have been applied to various fluids, such as steam [15,16] and CO_2 [17,18], as well as diverse geometries including turbine cascades [19,20] and converging–diverging nozzles [21]. Conversely, thermodynamic equilibrium condensation models are numerically more stable as they assume isothermal conditions between phases and can yield accurate results, particularly closer to the critical point, where the metastable region is narrow for both flashing [22,23] and condensing [24] flows. Within non-equilibrium models, a further distinction can be made between monodispersed and polydispersed droplet models.

Monodispersed droplet models consider a single average size of liquid droplets, neglecting the information and effects of the droplet size distribution. On the other hand, polydispersed droplet models account for the effects of droplet size distribution in the development of condensing flows.

The dispersed liquid phase can be simulated numerically using either a Lagrangian approach [25,26] or a Eulerian approach [27,28]. The method of moments (MOM) can be employed to compute the moments related to the droplet size distribution in both Lagrangian and Eulerian approaches [29]. The MOM can be enhanced by applying an n-point Gaussian quadrature [30], known as the quadrature method of moments (QMOM). QMOM is renowned for its accuracy and offers the advantage of not requiring prior knowledge of the shape of the droplet size distribution. QMOM has been successfully applied to supersonic low-pressure steam flows in nozzles [31,32] and turbine cascades [33], where the polydispersed droplet size distribution affects droplet growth, and its higher accuracy has been validated through experimental cases. Discrete methods, developed by Hounslow [34] and Litster [35], describe the droplet size distribution in terms of discrete size bins. Unlike QMOM, discrete methods are based on a predetermined shape of the droplet size spectrum, which can be defined by calculating low-order moments [36,37].

Polydispersed droplet models have primarily been applied to condensing gases in near-ideal conditions, such as low-pressure steam flows. However, for high reduced pressures, especially near the critical point, the non-ideality of the gas becomes significant and must be considered in the calculation of the droplet critical radius and nucleation rate under these thermodynamic conditions. At high reduced pressures, the surface tension decreases, reaching zero at the critical point, and the flow regime shifts towards a continuum flow characterized by low Knudsen numbers. These unique characteristics of two-phase flows profoundly influence the processes of droplet nucleation and growth, resulting in narrower nucleation regions and higher nucleation rates [17]. While these effects have been previously studied for monodispersed real gas flows, the application of QMOM and discrete methods to these flows, such as sCO_2 flows, is still lacking in the literature. Previous studies have focused on condensing gases in ideal or low-pressure conditions, neglecting the complexities introduced by high-pressure conditions and near-critical phenomena. As a result, there is a significant gap in understanding how polydispersed droplet models perform under these more complex and practically relevant conditions.

Therefore, this paper aims to explore the effects of polydispersed methods for flows that exhibit very different thermodynamic behavior and flow regimes compared to traditional low-pressure steam applications. Furthermore, the paper describes the development and evaluation of statistical approaches used to characterize the droplet size distribution within a commercial CFD solver. This involves a comprehensive comparison of the QMOM and discrete methods, emphasizing their applicability and accuracy in predicting droplet behavior in non-ideal gas conditions. This paper is structured as follows: First, the numerical framework is described, including the flow governing equations, the moments-based polydispersed droplets methods, the algorithms employed to solve the complex mathematical problems associated with them, and the integration of polydispersed methods with the non-equilibrium condensation model. Subsequently, numerical validation is conducted using experimental measurements for low-pressure and high-pressure steam, where the literature and experimental data are more abundant. The model is then applied to simulate CO_2 condensing flows near the critical point, comparing the behavior of QMOM with discrete methods based on normal and lognormal distributions. The simulations are conducted for converging–diverging nozzles and for a turbine cascade. The findings contribute to a better understanding of the complex behavior of condensing sCO_2 flows under thermodynamic non-equilibrium conditions, which has significant implications for the development of high-fidelity numerical tools applicable to a wide range of applications. By expanding the scope of polydispersed droplet models to high-pressure, near-critical conditions, this research offers a novel perspective and valuable contributions to the fields of non-equilibrium fluid dynamics and thermodynamics, paving the way for more accurate and efficient design and optimization of industrial systems involving supercritical fluids.

2. Numerical framework

The numerical simulations are conducted using the mixture model available in Ansys Fluent 2022 R2. A similar approach to that of Smolka et al. [23] has been previously validated for monodispersed droplet models in [17] and is employed here to simulate polydispersed droplet condensation models. The enthalpy-based energy equation is solved to compute the vapor temperature, in addition to the standard conservation equations for mass and momentum of the mixture. Mechanical equilibrium is considered between the phases, wherein slip velocities are neglected, as is typically done for droplets smaller than 1 μm. The computation of liquid droplet nucleation and growth involves solving the transport equations for the liquid volume fraction and the related moments. The full set of governing equations is presented below:

$$\frac{\partial \rho_m}{\partial t} + \nabla \bullet (\rho_m \boldsymbol{u_m}) = 0 \tag{1}$$

$$\frac{\partial \rho_m \boldsymbol{u_m}}{\partial t} + \nabla \bullet (\rho_m \boldsymbol{u_m} \boldsymbol{u_m}) = -\nabla p + \nabla \bullet (\bar{\bar{\tau}} + \overline{\overline{\tau_T}}) \tag{2}$$

$$\frac{\partial \alpha_v \rho_v h_v}{\partial t} + \nabla \bullet (\alpha_v \rho_v h_v \boldsymbol{u_m}) = \nabla \bullet \left(\Gamma_{eff} \nabla h_v\right) + S_{h1} + S_{h2} + S_{h3} + S_{h4} \tag{3}$$

$$\frac{\partial \alpha_l \rho_l}{\partial t} + \nabla \bullet (\alpha_l \rho_l \boldsymbol{u_m}) = S_{nuc} + S_{growth} \tag{4}$$

$$\frac{\partial \rho_m \mu_j}{\partial t} + \nabla \bullet \left(\rho_m \mu_j \boldsymbol{u_m}\right) = j \int_0^\infty r^{j-1} \rho_m \dot{r} \mu_0 f_\eta dr + J r^{*j} \tag{5}$$

where the diffusion coefficient in Eq. (3) is

$$\Gamma_{eff} = \left(\frac{k_{eff}}{\frac{\partial h}{\partial T}}\right)_{p=const.} = \frac{k + \frac{c_p \mu_T}{Pr_T}}{c_p} \tag{6}$$

and the turbulent Prandtl number is 0.85. Equations (3) and (5) are defined in Fluent as User-Defined Scalar (UDS) transport equations. The solution is obtained using the pressure-based coupled solver. The PRESTO! scheme is adopted for pressure spatial discretization, while the 2nd-order upwind scheme is used for all transport equations. The two-equation SST k-ω turbulence model [38] is used to close the RANS equations. In all cases, the total pressure is specified at the inlet boundary condition, and the static pressure is set at the outlet. Additionally, the total enthalpy at the inlet is specified using a User-Defined Function (UDF).

The transport equations of the moments can be reformulated using the n-point Gaussian quadrature introduced by McGraw [30]:

$$\frac{\partial \rho_m \mu_j}{\partial t} + \nabla \bullet \left(\rho_m \mu_j \boldsymbol{u_m}\right) = j \rho_m \sum_{i=1}^{n} r_i^{j-1} \dot{r}_i w_i + J r^{*j} \tag{7}$$

where the j-th order moment is defined as

$$\mu_j = \int_0^\infty r^j \mu_0 f_\eta dr = \sum_{i=1}^{n} r_i^j w_i. \tag{8}$$

Here, μ_0 is the number of droplets per unit mass, μ_1 is the sum of droplet radii per unit mass, μ_2 the sum of droplet interface areas per unit mass, μ_3 is the sum of droplet volumes per unit mass, and f_η is the droplet number density function (NDF). The computation of the n radii (r_i) and weights (w_i) can be carried out by solving the first $2n$ moment transport equations, with j ranging from 0 to $2n$-1, and using a moment-inversion

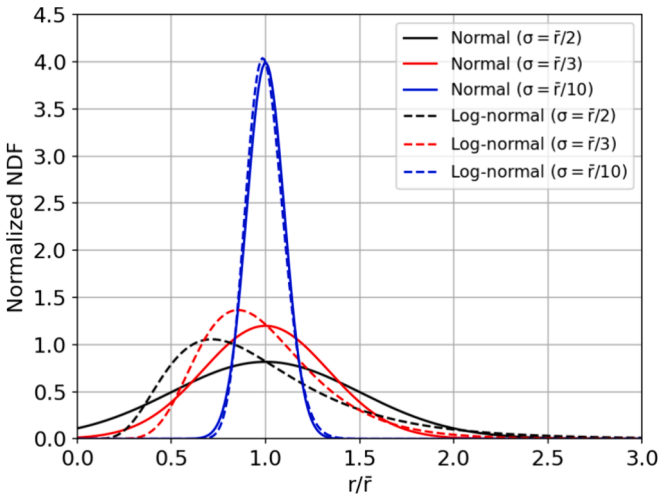

Fig. 1. Normalized NDF obtained using normal and lognormal distributions with varying standard deviations.

algorithm. In this study, $n = 3$ is chosen, as recommended in [39], for an optimal trade-off between accuracy and algorithm efficiency. Alternatively, the discrete method can be applied by assuming a priori the shape of the NDF, which necessitates solving the first three moments transport equations, as detailed in Section 2.2.

The source terms used in the transport equations are defined through UDFs and calculated as follows:

$$S_{h1} = \boldsymbol{u_m} \bullet \nabla p \tag{9}$$

$$S_{h2} = (\mu + \mu_T)\left\{2\left[\left(\frac{\partial u}{\partial x}\right)^2 + \left(\frac{\partial v}{\partial y}\right)^2\right] + \left(\frac{\partial u}{\partial y} + \frac{\partial v}{\partial x}\right)^2 - \frac{2}{3}(\nabla \bullet \boldsymbol{u_m})^2\right\} - \frac{2}{3}\rho K \nabla \bullet \boldsymbol{u_m} \tag{10}$$

$$S_{h3} = -\rho \boldsymbol{u_m} \bullet \nabla K \tag{11}$$

$$S_{h4} = -\left(S_{nuc} + S_{growth}\right)h_v + Q_{conv} \tag{12}$$

$$Q_{conv} = \left(S_{nuc} + S_{growth}\right)h_{fg} - \alpha_l \rho_l \boldsymbol{u_m} \bullet \nabla h_l \tag{13}$$

$$S_{nuc} = \frac{4}{3}\pi r^{*3}\rho_l J \tag{14}$$

$$S_{growth} = 4\pi\rho_l\rho_m \sum_{i=1}^{n} r_i^2 \dot{r}_i w_i. \tag{15}$$

Here, S_{h1} is the mechanical energy, S_{h2} is the irreversible dissipation of the kinetic energy variations, S_{h3} is the dissipation of the turbulent kinetic energy, S_{h4} is the energy transfer due to condensation, S_{nuc} is the mass transfer due to droplet nucleation, and S_{growth} is the interfacial mass transfer between phases.

The fluid properties of the vapor phase are calculated from the static pressure and the static enthalpy up to the spinodal limit. Conversely, the dispersed liquid phase is assumed to be in saturated conditions, requiring only the pressure as input. The Multispecies User-Defined Real Gas Model (UDRGM) accesses and interpolates property look-up tables generated by an in-house Python code that utilizes the multiparameter equation of state based on the Helmholtz energy [40,41], available in Refprop thermodynamic libraries [42]. Further details regarding the property calculations performed through UDRGM can be found in [17].

The radii and weights used to compute the source terms associated with droplet growth in Eqs. (7) and (15) can be determined in various ways for polydispersed models. QMOM is renowned for its high accuracy and does not require a priori knowledge of the shape of the NDF. However, it necessitates the use of complex and time-consuming algorithms for moment-inversion, which may lead to mathematical complications such as non-realizability of moments [43], and it relies on a limited number of discrete radii, typically set to 3. On the other hand, discrete methods are much simpler to implement, avoid mathematical issues, and allow for the use of a larger number of discrete radii. However, they fix the NDF to a predetermined shape, which can introduce inaccuracies in the results. This paper compares QMOM with discrete methods based on normal and lognormal NDFs. The mathematical definitions of both methods are provided in the following subsections.

2.1. Quadrature method of moments

The QMOM requires a moment-inversion algorithm, upon which the overall efficiency and stability of the simulation depend, with up to 20 % of CPU time required for it [32]. Wheeler's algorithm [44] is used due to its enhanced stability compared to other algorithms such as the product-difference method [45]. Wheeler's algorithm is implemented in a UDF as outlined in [46], yielding the Jacobi matrix whose elements are computed based on the moments μ_j:

$$\boldsymbol{J}_3 = \begin{bmatrix} a_1 & b_1 & 0 \\ b_1 & a_2 & b_2 \\ 0 & b_2 & a_3 \end{bmatrix}. \tag{16}$$

The radii and weights can be calculated by solving the eigenvalue problem for the Jacobi matrix as

$$r_i = \lambda_i \tag{17}$$

$$w_i = \mu_0 v_{1i}^2 \tag{18}$$

where λ_i are the eigenvalues and v_{1i} are the first elements of the eigenvectors. Since the use of external libraries is restricted in UDFs, an eigen decomposition algorithm is implemented to compute both eigenvalues and eigenvectors of the Jacobi matrix. The symmetric tridiagonal QL algorithm developed by the Java matrix library JAMA [47] and described in [48] is used, yielding eigenvalues and eigenvectors as:

$$\boldsymbol{J}_3 = \boldsymbol{v} \bullet \boldsymbol{\lambda} \bullet \boldsymbol{v}^T \tag{19}$$

where $\boldsymbol{\lambda}$ is a diagonal matrix containing the eigenvalues, and $\boldsymbol{v}$ is the orthogonal matrix containing the eigenvectors.

2.2. Discrete methods

Discrete methods represent the NDF in terms of a set of discrete size bins. Unlike QMOM, discrete methods require knowledge of the NDF shape in advance. In this paper, two distributions are considered: the normal and the lognormal distributions. These are chosen as they are common statistical distributions used to describe droplet or particle distributions [36,37]. The parameters required to define these distributions are the mean radius and the standard deviation, which can be estimated from the first three moments. Normalized NDFs based on normal and lognormal distributions are plotted for different standard deviation over mean radius values in Fig. 1. The NDF is integrated over a predefined radius range, for instance, from 0 to $m \bullet r_{10}$, where m must be large enough to cover the NDF curve such that the chosen NDF satisfies the following equation:

$$\int_0^{m \bullet r_{10}} f_\eta dr \approx 1. \tag{20}$$

However, m should be also as small as possible to minimize the number of radius discretization points required to achieve a satisfactory resolution. In this work, $m = 3$ is chosen, which represents a good trade-off, as shown in Fig. 1, as it covers the entire integration area of the NDF even for large values of the standard deviation. Once the NDF shape and

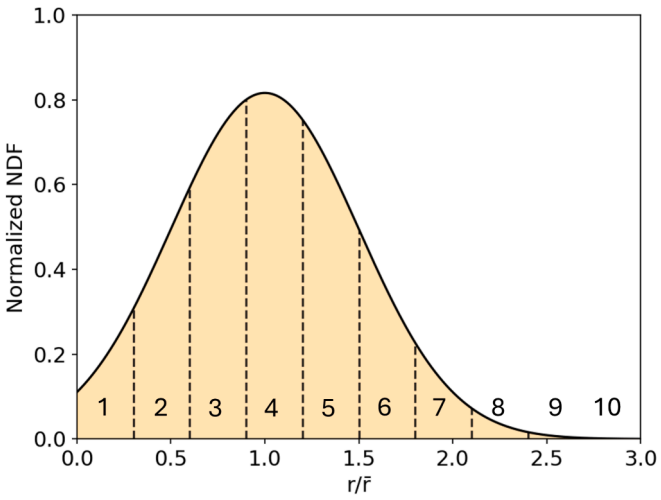

Fig. 2. Example of NDF discretization utilized in discrete methods.

Table 1
Thermodynamic and flow regime parameters for nozzle cases.

Cases	Fluid	T_0 [°C]	p_0 [bar]	z_0	Kn
1	LP steam	107.40	0.7839	0.989	2–6
2	LP steam	103.80	0.7839	0.989	1.5–5
3	HP steam	365.53	100.7	0.805	0.03–0.1
4	HP steam	342.05	100.7	0.762	0.02–0.08
5	CO_2	36.85	58	0.677	0.003–0.015
6	CO_2	68.00	120	0.518	0.003–0.015

Table 2
Thermodynamic boundary conditions for turbine cascade cases.

Cases	Fluid	T_0 [°C]	p_0 [bar]	p_{out} [bar]	p_0/p_{out}
7	LP steam	99	1.14	0.60	1.90
8	LP steam	106	1.00	0.42	2.38
9	CO_2	36	65	34.21	1.90
10	CO_2	40	65	27.30	2.38

the integration range are chosen, the NDF is divided into n portions as shown in Fig. 2 for $n = 10$, and each area can be integrated to compute the corresponding weight, i.e., the number of droplets per unit mass of each region.

If a Gaussian distribution is assumed for the NDF, the mean radius r_{10} and the standard deviation σ_{gauss} can be calculated using the first three moments as:

$$r_{10} = \frac{\mu_1}{\mu_0} \tag{21}$$

$$\sigma_{gauss} = \sqrt{\frac{\mu_2}{\mu_0} - \left(\frac{\mu_1}{\mu_0}\right)^2}. \tag{22}$$

The NDF is given by:

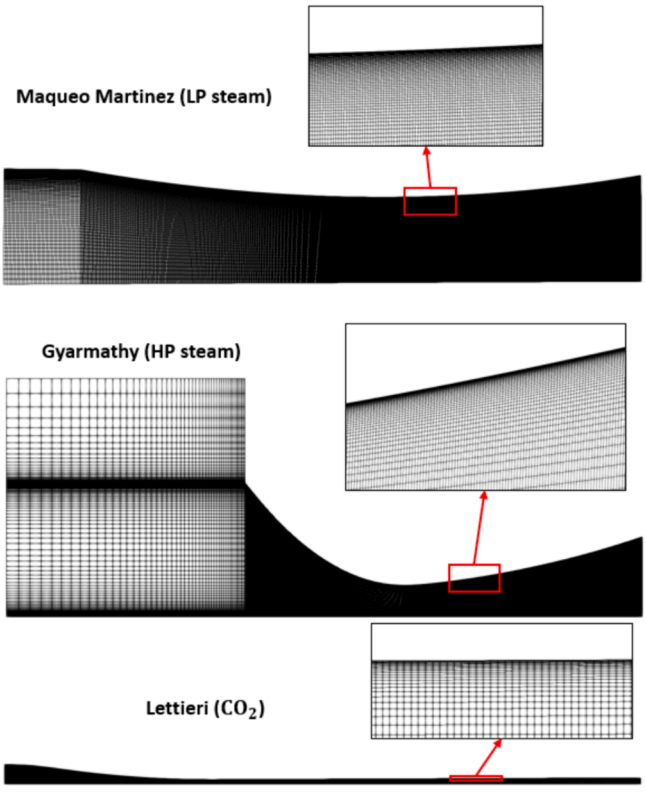

Fig. 4. Grids of the three nozzle geometries (not to scale) and details of the near-wall region.

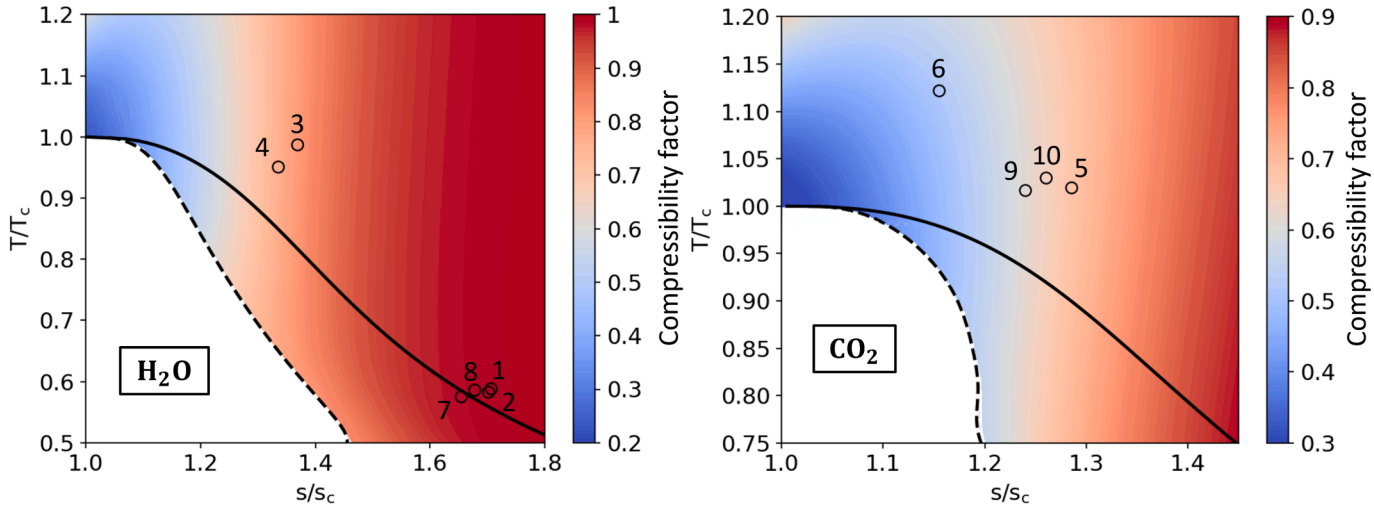

Fig. 3. Inlet thermodynamic point on a non-dimensional *T-s* diagram overlaid to compressibility factor contours. Solid and dashed lines denote the saturation curve and spinodal limit, respectively.

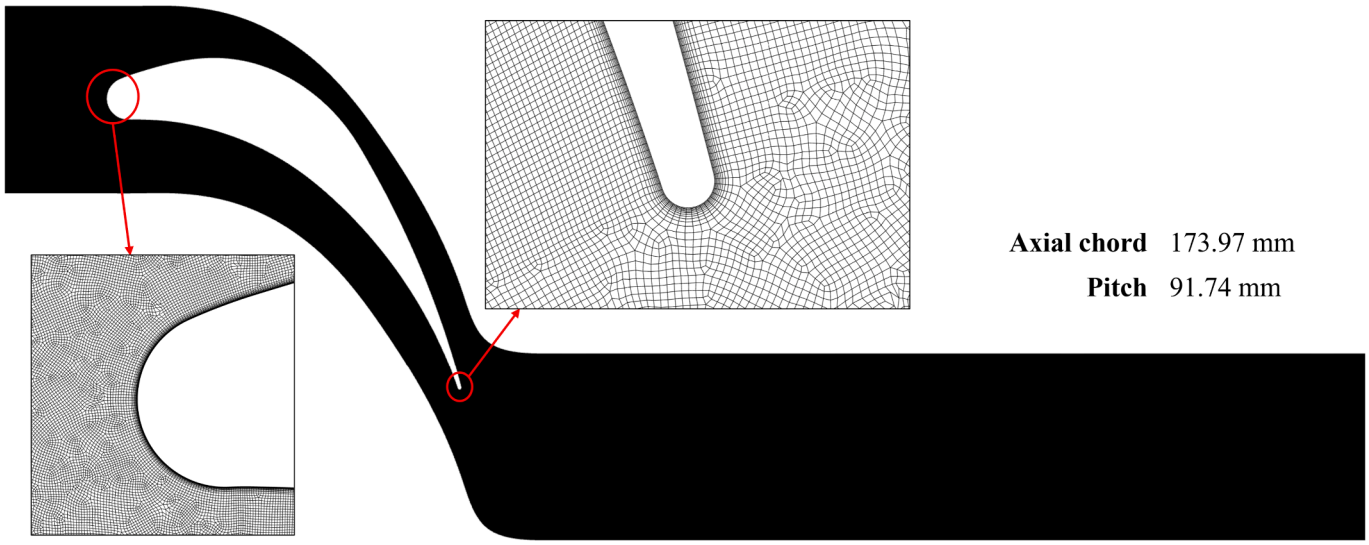

Fig. 5. Grid of the turbine cascade geometry and details of the leading and trailing edges.

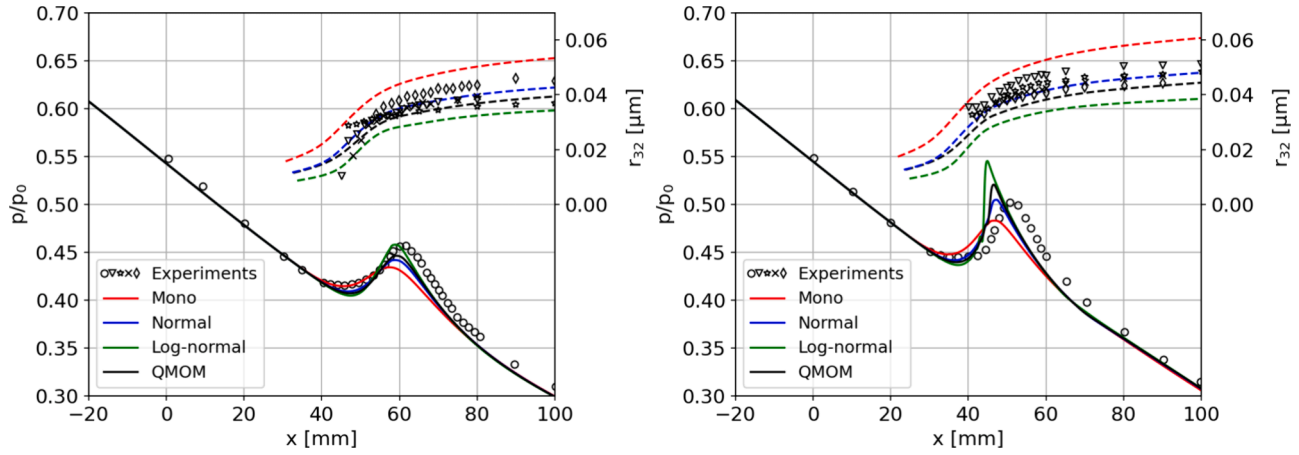

Fig. 6. Pressure and r_{32} distributions along the streamwise direction for LP steam: case 1 (left) and case 2 (right).

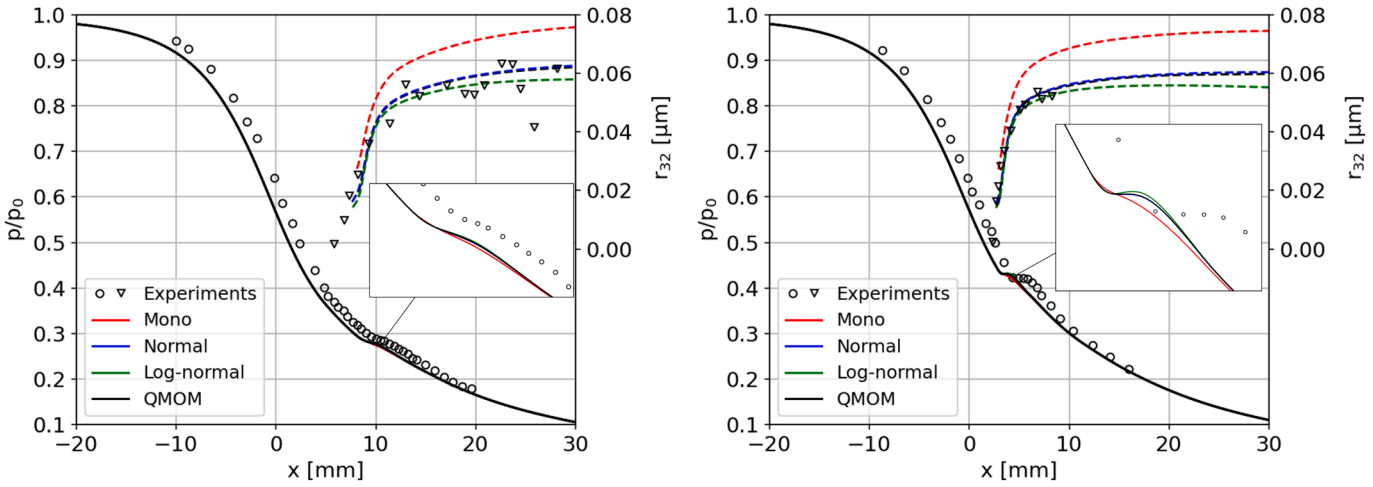

Fig. 7. Pressure and r_{32} distributions along the streamwise direction for HP steam: case 3 (left) and case 4 (right).

$$f_{\eta,gauss}(r) = \frac{1}{\chi\sigma_{gauss}\sqrt{2\pi}}\exp\left(-\frac{(r-r_{10})^2}{2\sigma_{gauss}^2}\right) \quad (23)$$

$$\chi = \frac{1}{2}\left[erf\left(\frac{\sqrt{2}}{2}\frac{r_{10}}{\sigma_{gauss}}\right) - erf\left(\frac{\sqrt{2}}{2}\frac{r_{10}(1-m)}{\sigma_{gauss}}\right)\right] \quad (24)$$

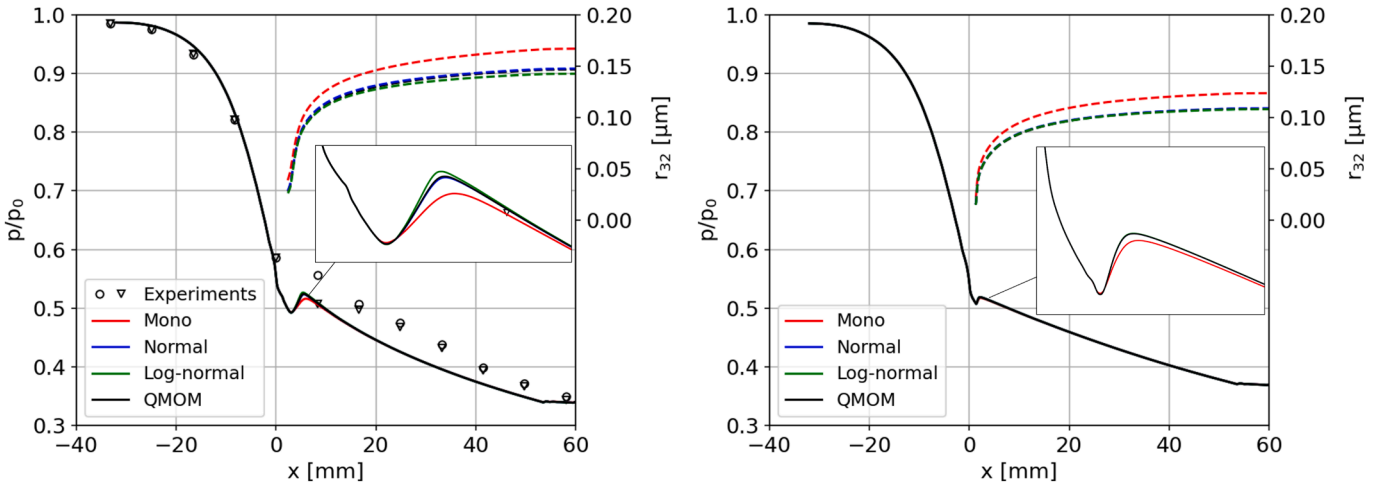

Fig. 8. Pressure and r_{32} distributions along the streamwise direction for CO_2: case 5 (left) and case 6 (right).

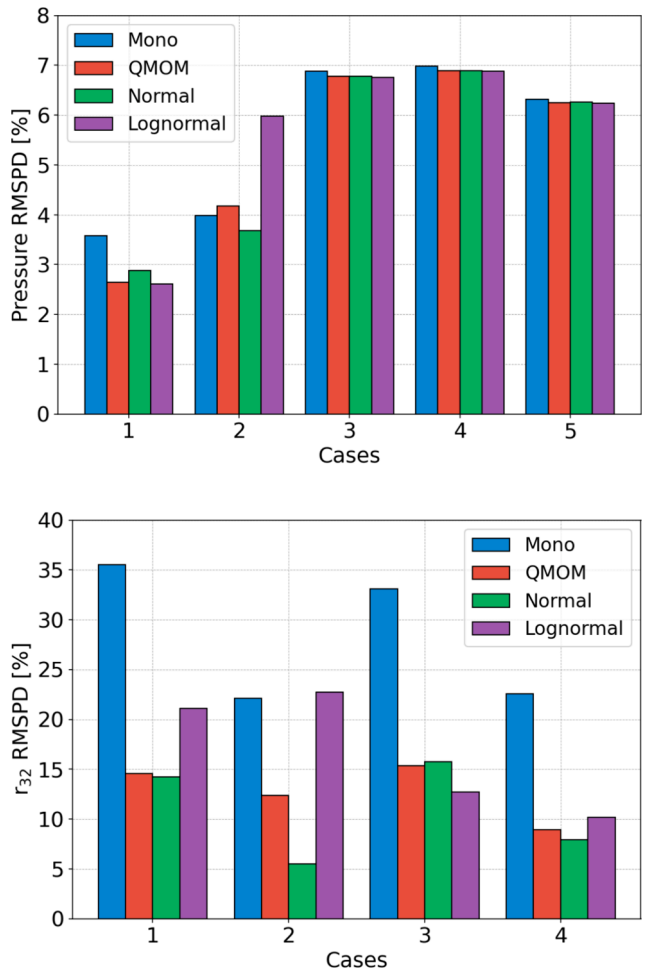

Fig. 9. RMSPD for nozzle cases: pressure (top) and r_{32} (bottom).

where χ is calculated to satisfy Eq. (20). This coefficient recovers the lost integration area for negative radii and radii larger than the upper integration limit $m \bullet r_{10}$. The latter is a case that should be avoided by choosing m large enough, as described above in the description of discrete methods. Therefore, the radius and weight for a generic interval $[a, b]$ assuming a Gaussian NDF can be calculated in a closed form as

$$r_i = \frac{a+b}{2} \tag{25}$$

$$w_{i,gauss} = \mu_0 \int_a^b f_{\eta,gauss} dr = \mu_0 \frac{\operatorname{erf}\left(\frac{\sqrt{2}}{2}\frac{(r_{10}-a)}{\sigma_{gauss}}\right) - \operatorname{erf}\left(\frac{\sqrt{2}}{2}\frac{(r_{10}-b)}{\sigma_{gauss}}\right)}{2\chi}. \tag{26}$$

The NDF is also modeled assuming a lognormal distribution, whose main parameters to describe it can be derived from the normal mean radius and standard deviation as:

$$r_{log} = \frac{r_{10}^2}{\sqrt{r_{10}^2 + \sigma_{gauss}^2}} \tag{27}$$

$$\sigma_{log} = \sqrt{\ln\left(1 + \frac{\sigma_{gauss}^2}{r_{10}^2}\right)} \tag{28}$$

where r_{log} is the median and σ_{log} is the shape parameter. The NDF is defined as

$$f_{\eta,log}(r) = \frac{1}{r\sigma_{log}\sqrt{2\pi}} \exp\left(-\frac{(\ln r - \ln r_{log})^2}{2\sigma_{log}^2}\right). \tag{29}$$

No correction coefficient is applied in this case since, for large standard deviations, the curve is contained within the fixed range of radii. A closed-form solution of the integral of the lognormal NDF does not exist. Therefore, the calculation of the weights requires numerical integration, which significantly increases the computational effort of the simulation, as will be demonstrated in Section 4. Applying the trapezoidal integration rule, the weight can be calculated for a generic interval $[a, b]$ with a uniform discretization grid as:

$$w_{i,log} = \mu_0 \int_a^b f_{\eta,log} dr \approx \mu_0 \frac{\Delta r}{2} \sum_{k=1}^{N} \left(f_{\eta,log}(r_{k-1}) + f_{\eta,log}(r_k)\right) \tag{30}$$

$$\Delta r = \frac{b-a}{N}. \tag{31}$$

In this paper, each of the ten radius intervals of the lognormal NDF is integrated using the trapezoidal rule with N=10, resulting in a radius resolution Δr for the numerical integration equal to 1 % of the overall radius range considered.

2.3. Non-equilibrium condensation model

The non-equilibrium condensation model describes the nucleation

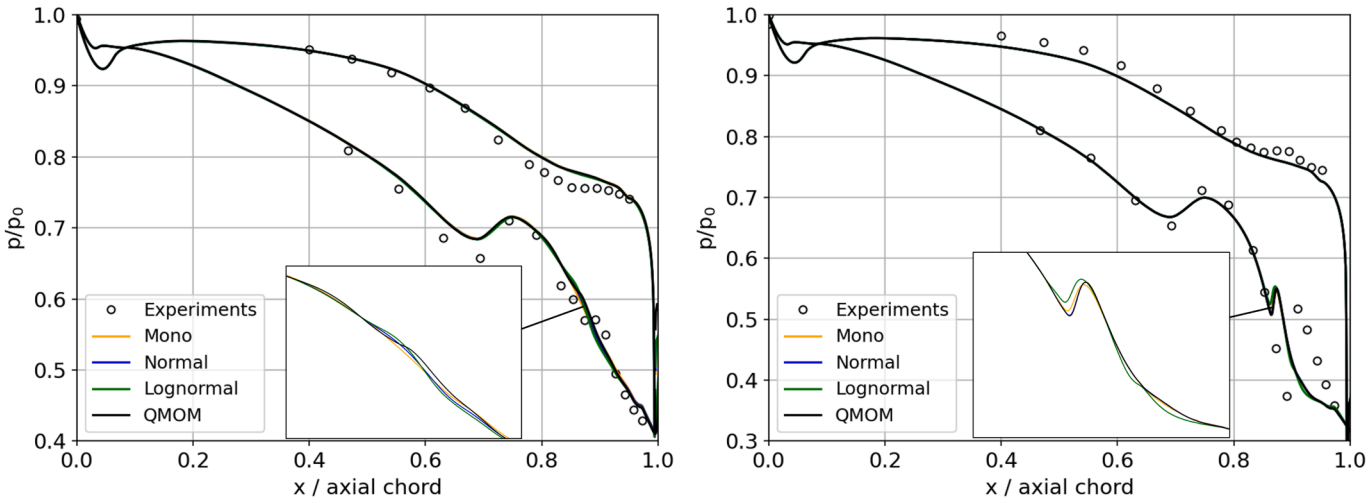

Fig. 10. Pressure distributions along the blade profile for LP steam: case 7 (left) and case 8 (right).

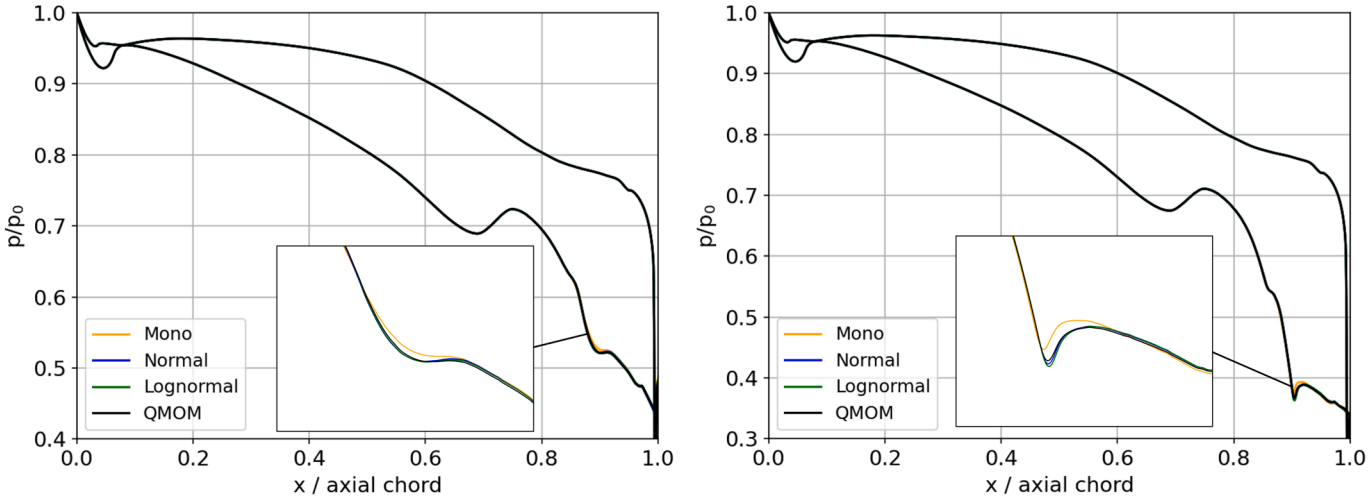

Fig. 11. Pressure distributions along the blade profile for CO_2: case 9 (left) and case 10 (right).

Table 3
CPU time per iteration and percentage difference (vs. Mono) calculated for case 7.

Method	CPU time per iteration [s]	Percentage difference (vs. Mono) [%]
Mono	0.62	–
Normal	0.82	+32.3
QMOM	0.92	+48.4
Lognormal	2.81	+353.2

and subsequent growth of dispersed liquid droplets in a supersaturated vapor flow. According to the Classical Nucleation Theory (CNT) proposed by Becker and Döring [49], the nucleation rate is calculated as:

$$J_{CNT} = \frac{\rho_v^2}{\rho_l}\sqrt{\frac{2\sigma}{\pi M_m^3}}\exp\left(-\frac{4}{3}\frac{\pi r^{*2}\sigma}{k_b T_v}\right). \tag{32}$$

The CNT is modified by applying Courtney's correction [50], which divides the nucleation rate by the supersaturation ratio. However, in this paper, an exponent is applied to reduce the effects of Courtney's correction and achieve a better match with experimental results:

$$J = \frac{z_v}{S^{0.5}} J_{CNT} \tag{33}$$

$$S = \frac{p}{p_s(T_v)}. \tag{34}$$

The critical radius can be calculated for a real gas as described in [17]:

$$r^* = \frac{2\sigma}{z_v \rho_l R T_v \ln S - p\left(1 - \frac{1}{S}\right)}. \tag{35}$$

The droplet growth rate depends on the droplet size and therefore must be calculated for each discretized radius considered in the QMOM or discrete method. The correlation proposed by Gyarmathy [51] to model the convective heat transfer at the droplet interface can be used to calculate the droplet growth rate as:

$$\dot{r}_i = \frac{k_v(T_s - T_v)}{\rho_l h_{fg} r_i (1 + 3.18 Kn_i)} \tag{36}$$

$$Kn_i = \frac{mfp}{2r_i} = \frac{\mu_v}{2r_i\rho_v}\sqrt{\frac{\pi M_m}{2k_B T_v}}. \tag{37}$$

Here, *Kn* is the Knudsen number, which defines the degree of rarefaction of the flow.

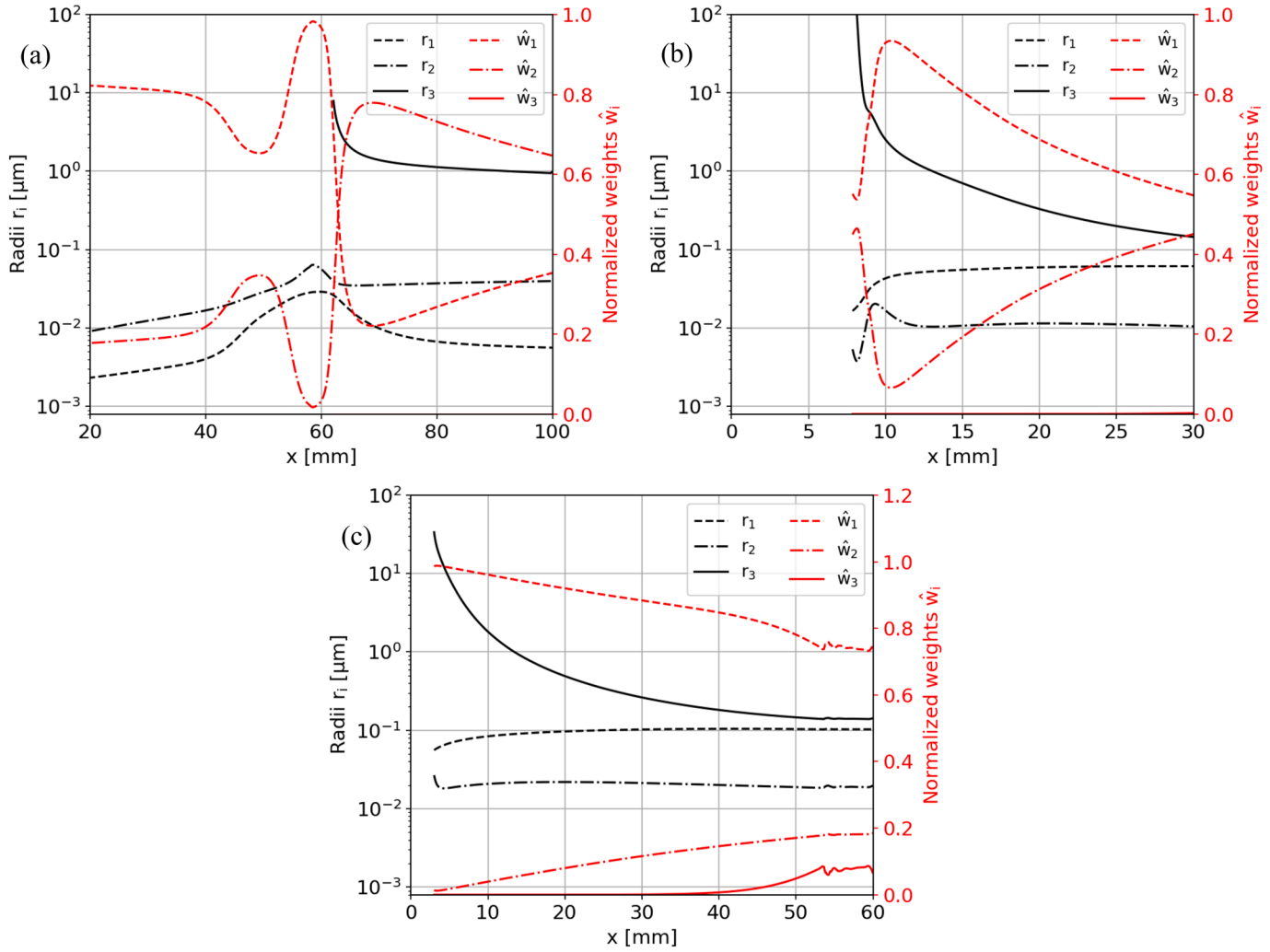

Fig. 12. Radii and normalized weights distributions along the streamwise direction: (a) LP steam case 1, (b) HP steam case 3 and (c) CO_2 case 6.

3. Description of the test cases

The numerical and physical models are applied to low-pressure (LP) steam, high-pressure (HP) steam and CO_2 flows in 2D nozzle geometries and a turbine cascade. Although the analysis aims to focus on sCO_2 flows, it is beneficial to validate the polydispersed droplet condensation models for steam cases where there is a larger availability of experiments. Additionally, the effect of the degree of flow rarefaction and the flow expansion rate can be studied under different thermodynamics conditions and nozzle geometries. Three test cases involving 2D nozzle geometries are selected, and their inlet thermodynamic conditions and Knudsen number ranges are reported in Table 1. The test cases are sourced from Maqueo Martinez et al. [52] for LP steam, from Gyarmathy's nozzle 4/B [53] for HP steam and from Lettieri et al. [54] for CO_2. Additionally, case 6 is simulated for studying the non-equilibrium behavior of CO_2 very close to the critical point, even though it was not studied experimentally. Furthermore, the turbine cascade from Dykas et al. [55,56] is simulated with LP steam, for which experimental measurements are available, as well as CO_2, and the boundary conditions are reported in Table 2. Steam and CO_2 flows through the turbine cascade are simulated by applying the same expansion ratios to obtain similar flow features, enabling a meaningful comparison of performance. The inlet thermodynamic points of each case are depicted in temperature-specific entropy diagrams in Fig. 3. The fluid is in a superheated or supercritical state for each point at the inlet section, except for case 7, which has a subcooling degree of 4.3 °C, as per Dykas' experiments. This leads to condensation occurring in the subsonic region of the blade channel.

The nozzles from Maqueo Martinez and Lettieri are simulated with the top side defined as a no-slip wall and the bottom side as a symmetry. The nozzle from Gyarmathy is non-symmetric, and both upper and lower sides are defined as no-slip walls. These nozzles have previously been investigated with monodispersed droplet models in [17], where grid independence studies were carried out.

The simulated grids of the nozzles are represented in Fig. 4, along with details of the near-wall region. The turbine cascade from Dykas is shown in Fig. 5 and is simulated applying periodic boundary conditions at the top and bottom sides of the fluid domain, while the blade profile is defined as a no-slip wall. The fluid domain at the outlet of the blade channel is extended axially by more than twice the length of the axial chord to prevent wave reflections from influencing the upstream flow. The grid independence study of the blade cascade has been conducted simulating three grids with different levels of refinement. It was found that the two finest grids, consisting of 246 k and 493 k cells respectively, yielded negligible differences in the results. Specifically, the largest relative differences observed in the distributions of static pressure and mean droplet size, calculated at a section downstream of the blade, were 0.2 % and 1.5 %, respectively. For each grid, it was ensured that the wall y^+ remained below 30, and scalable wall functions were automatically used by the solver when the viscous sublayer was not fully solved. Further refinements of the near-wall region aiming to solve the whole boundary layer led to numerical convergence issues. Specifically, in

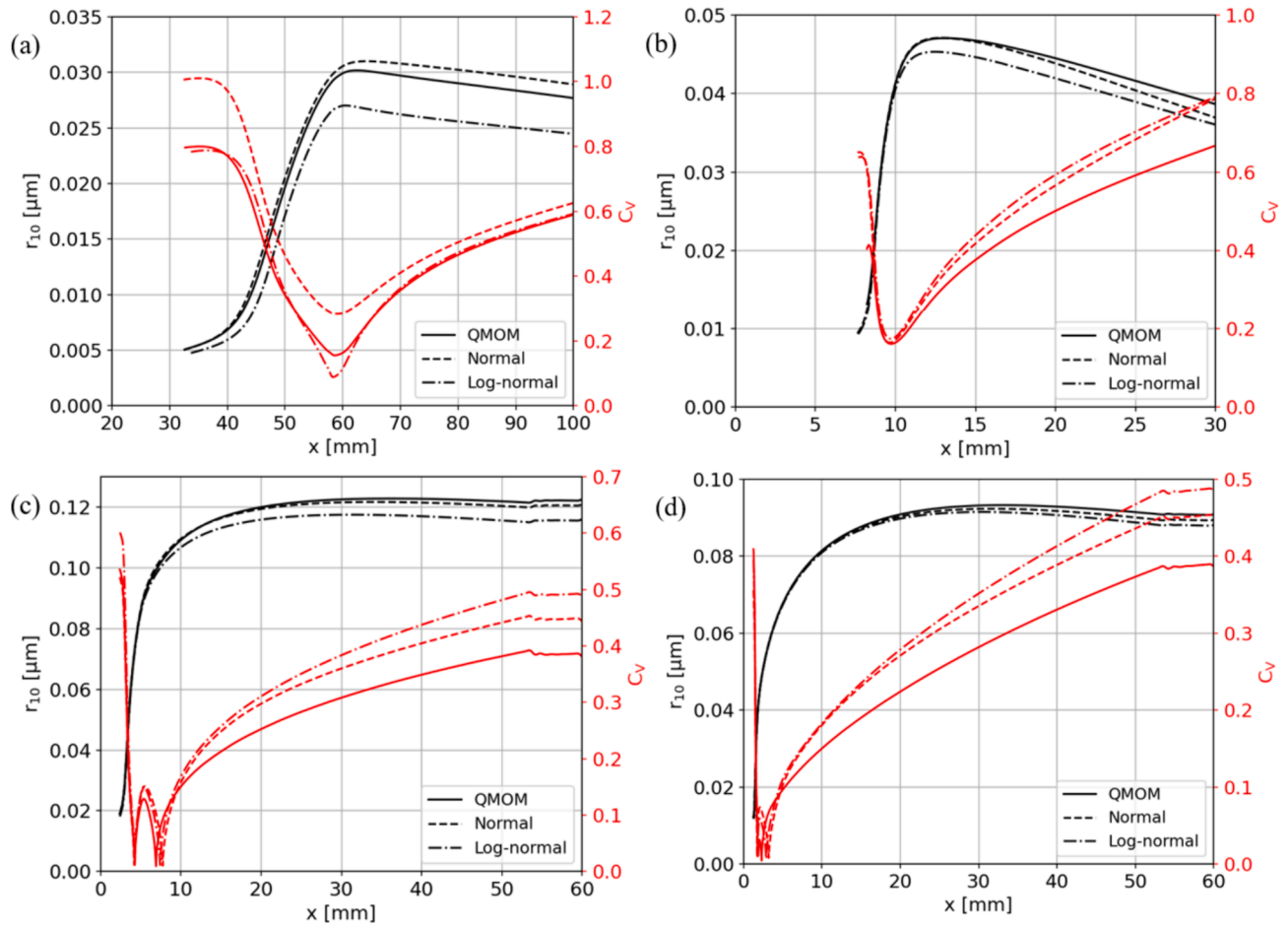

Fig. 13. r_{10} and C_V distributions along the streamwise direction: (a) LP steam case 1, (b) HP steam case 3, (c) CO_2 case 5 and (d) CO_2 case 6.

Table 4
Expansion rate in the nozzle divergent section and average slope in the streamwise direction of C_V for QMOM results.

Cases	Expansion rate (divergent) [s^{-1}]	$\frac{\partial C_V}{\partial x}$ [m^{-1}]
1	4–8 • 10^3	12.5
2	3–8 • 10^3	9.2
3	4–5 • 10^4	25.0
4	4–5 • 10^4	23.2
5	2–5 • 10^3	8.6
6	1–2 • 10^3	7.8

turbine cascade cases, numerical divergence occurred at the trailing edge during the time-marching solution when the cell height close to the blade wall was too small. Further analysis is necessary to determine the root cause of this numerical issue.

4. Results and discussion

4.1. Model validation

The test cases presented in Section 3 are simulated to validate the numerical models. Both QMOM and discrete methods based on normal and lognormal distributions are applied. Fig. 6 shows the pressure and Sauter radius distributions along the streamwise direction for cases 1 and 2 with LP steam. The Sauter radius is a statistical parameter defined as the diameter of a sphere that has the same volume-to-surface area ratio as the droplets in the domain. The Sauter radius is calculated based on moments as follows:

$$r_{32} = \frac{\mu_3}{\mu_2}. \tag{38}$$

For LP steam, the Knudsen numbers encountered are higher than unity, suggesting a transitional or free molecular flow regime. This means that the droplet growth rate model strongly relies on the Knudsen number evolution in the metastable region for each droplet size group. It is observed that the monodispersed model predicts an earlier pressure rise due to the latent heat release, and the pressure peak is lower than that obtained with polydispersed models. Moreover, the r_{32} is overestimated for the monodispersed model. Comparing the polydispersed models, the normal NDF and QMOM better agree with the experiments, both in terms of calculated pressure and droplet size. On the other hand, the lognormal NDF tends to overpredict the pressure peak and underpredict the r_{32}. Increasing the steam inlet pressure enhances the nonideality of the vapor phase and leads to a slip flow regime, with Knudsen numbers lower than 0.1. The results obtained for HP steam in cases 3 and 4 are shown in Fig. 7. Similar outcomes to those discussed for LP steam are observed, with the monodispersed model overestimating r_{32} and underestimating the condensation pressure rise. On the other hand, the polydispersed models show better agreement with experiments for r_{32}, although some differences are noted in the pressure distribution in both the convergent and divergent sections. These differences suggest a shift of the pressure curve in the axial direction. In condensing CO_2 cases, the Knudsen number reduces even further, and they are classified as continuum flows. Fig. 8 shows the results obtained in cases 5 and 6. In case 6, where condensation occurs very close to the critical point leading to high nucleation rates and low droplet surface tensions, the monodispersed model shows good accuracy for the pressure rise, but still

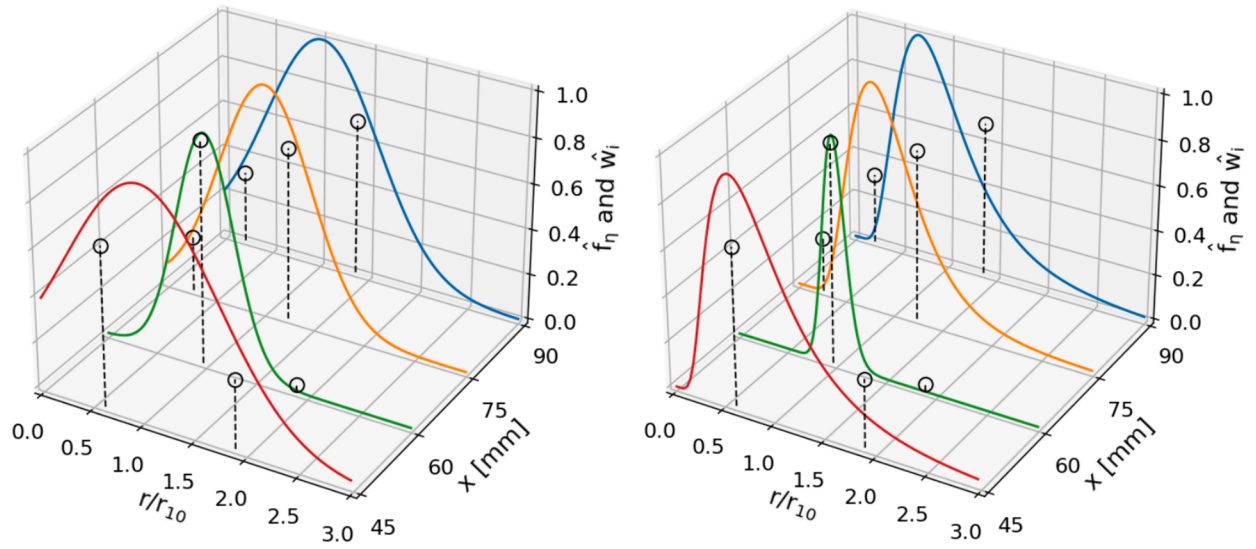

Fig. 14. Normalized weights from QMOM (black circles with dashed lines) and NDFs scaled to unity (solid lines) along the nozzle axis for LP steam case 1. Normal NDF (left) and lognormal NDF (right).

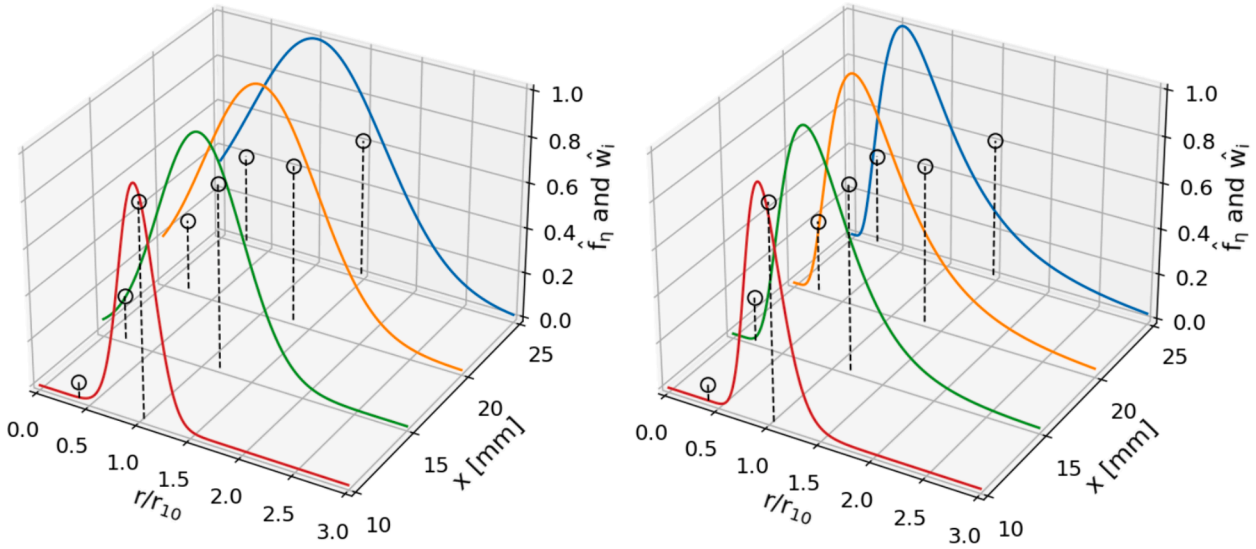

Fig. 15. Normalized weights from QMOM (black circles with dashed lines) and NDFs scaled to unity (solid lines) along the nozzle axis for HP steam case 3. Normal NDF (left) and lognormal NDF (right).

overpredicts r_{32} compared to polydispersed models. Since droplet size measurements are not available for CO_2, it is not possible to state which approach is more accurate for these cases. The similar behavior between QMOM and the normal NDF is confirmed, and it is observed that the lognormal NDF tends to predict results like other methods for thermodynamic conditions closer to the critical point.

The difference between experimental results and various condensation models for nozzle cases is quantified by calculating the root mean square percentage difference (RMSPD). This calculation considers the difference between each experimentally measured point and the value calculated by CFD at the closest node in the streamwise direction along the nozzle, as follows:

$$RMSPD = \sqrt{\frac{1}{N_{exp}} \sum_{i=1}^{N_{exp}} \left(\frac{\phi_{exp,i} - \phi_{CFD,i}}{\phi_{exp,i}} \right)^2}. \tag{39}$$

The RMSPD of pressure and r_{32} are reported in Fig. 9. The results indicate that the QMOM and normal NDF perform better overall than the monodispersed model and the lognormal NDF. In LP steam, cases 1 and 2, the RMSPDs for the r_{32} range between 5.5 % and 14.2 % for the normal NDF and between 12.4 % and 14.6 % for QMOM, increasing up to 22.8 % for the lognormal NDF and up to 35.5 % for the monodispersed model. For HP steam, cases 3 and 4, all polydispersed models perform similarly, with r_{32} RMSPDs between 7.9 % and 15.8 %, while they rise to 33.1 % for the monodispersed simulations. The similarities observed among the various polydispersed distributions at high reduced pressures can be attributed to the droplet nucleation process, which remains unaffected by droplet sizes and plays a more significant role than droplet growth in determining droplet sizes at higher reduced pressures.

The pressure distributions on the blade profile from the turbine cascade of Dykas, obtained with monodispersed and polydispersed models, are shown in Fig. 10 for LP steam cases 7 and 8 and compared with static pressure measurements available in [56]. A first pressure rise is observed on the blade suction surface due to a separation region (x/b_x 0.69), which is well captured by CFD. A second pressure rise is observed on the blade suction side (x/b_x 0.83) and is underpredicted by CFD,

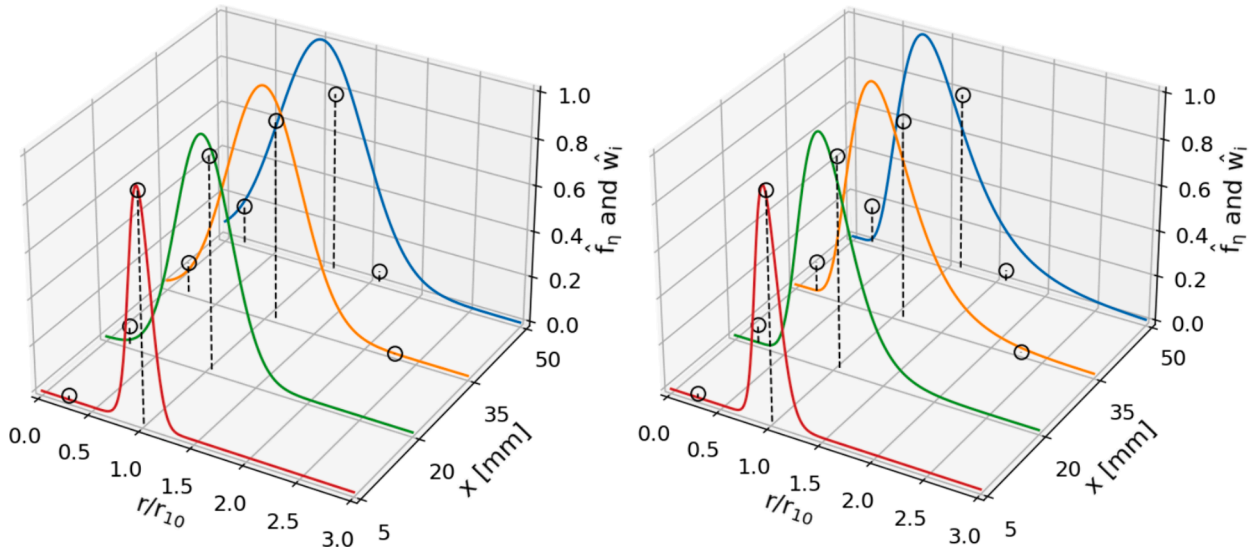

Fig. 16. Normalized weights from QMOM (black circles with dashed lines) and NDFs scaled to unity (solid lines) along the nozzle axis for CO_2 case 6. Normal NDF (left) and lognormal NDF (right).

particularly for case 8 where higher Mach numbers are involved. This pressure rise is caused by the aerodynamic shock wave generated at the trailing edge and reflected on the suction side, along with the condensation latent heat release. Monodispersed and polydispersed models do not present significant variations in terms of pressure distributions in both cases, although the lognormal NDF slightly anticipates the second pressure rise. The same blade profile has been simulated using CO_2 in cases 9 and 10 by applying the same expansion ratios used for steam and inlet stagnation thermodynamic conditions to obtain a similar location of the condensation onset. The pressure distributions on the blade are shown in Fig. 11. The first pressure rise due to the separation region is predicted similarly to steam. Conversely, two additional separate pressure rises are observed on the suction side: one related to the condensation heat release (x/b_x 0.86) and the second related to the trailing edge shock wave reflection (x/b_x 0.90). The latter is predicted to reflect on the blade suction side at a larger angle compared to steam, and thus further downstream on the blade surface. Even for CO_2, monodispersed and polydispersed models predict similar pressure distributions, except for the pressure rise related to the trailing edge shock wave reflection, which is slightly anticipated by the monodispersed model. Further analysis and discussion of the results of the Dykas turbine cascade are reported in Section 4.3.

The computational effort for monodispersed and polydispersed CFD simulations is calculated in terms of average CPU time per iteration. The results obtained for the turbine cascade operating with steam (case 7) are reported in Table 3. The lowest computational effort is found for the monodispersed model, as expected, while it slightly increases for the normal NDF and QMOM by 32.3 % and 48.4 %, respectively, compared to the monodispersed case. A significant increase in the CPU time is observed for the lognormal distribution (+353.2 %), which is caused by the numerical integration of the NDF required for this method.

4.2. NDF evolution in nozzle geometries

The NDF varies in space following the evolution of the moments. For QMOM, it is possible to plot the radii and weights along the streamwise direction calculated using the moment-inversion algorithm described in Section 2.1, as shown in Fig. 12 for cases 1, 3 and 6. Cases 2, 4 and 5 exhibit similar results to cases 1, 3 and 6, respectively. The calculation of the radii was lower bounded to 1 nm, which is approximately the size of the critical radius, to avoid numerical issues. The highest calculated value of the radius is much larger than the mean radius, but its corresponding weight is close to zero, which results in $\hat{w}_3$ almost overlapping the x-axis. This can be attributed to the non-realizability issues discussed in Section 2.1, indicating that this set of radius and weight does not affect the droplet growth process.

The mean radius (r_{10}) and the coefficient of variation (C_V) are moment-based statistical parameters useful for describing the droplet number distributions obtained for the considered polydispersed models. The mean radius is the arithmetic mean of the droplet radii and is defined in Eq. (21), while the coefficient of variation, a measure of relative variability, is defined in Eq. (40).

$$C_V = \frac{\sigma_{gauss}}{r_{10}}. \tag{40}$$

A low C_V indicates that the NDF is narrow and close to the mean radius, thus the droplets are monodispersed, while a high C_V indicates that the NDF is spread over a wider range relative to the mean radius, providing a quantitative measure of polydispersed effects. The distributions along the streamwise direction of r_{10} and C_V are represented in Fig. 13 for cases 1, 3, 5, and 6. Cases 2 and 4 are omitted as they exhibit similar results to cases 1 and 3, respectively. As a general observation, when the model predicts higher values of r_{10}, C_V is lower, and vice versa. At the beginning of the condensation region, the C_V values are very high for a relevant space interval in case 1, which decreases for the other cases. Although similar values of C_V are observed for LP steam and CO_2 cases, the polydispersed effects have a much greater impact in LP steam. LP steam flows are characterized by larger Knudsen numbers, where droplet development is significantly affected by their sizes. In contrast, CO_2 flows are characterized by very low Knudsen numbers, where droplet size distributions minimally affect droplet growth.

The expansion rate is a key parameter affecting the location of the Wilson point, which is the thermodynamic point in the metastable region where condensation occurs. In fact, the higher the expansion rate, the deeper the expansion penetrates the metastable region before nucleation begins. The expansion rate achieved in the nozzle divergent section is also important for quantitatively describing how quickly the flow is expanded in a certain space interval and is defined as:

$$\dot{p} = -\frac{|\boldsymbol{u}_m|}{p}\frac{dp}{dx}. \tag{41}$$

Both the expansion rate and the average slope of C_V along the streamwise direction obtained with QMOM are reported for the studied cases in Table 4. It is quite evident that the expansion rate strongly

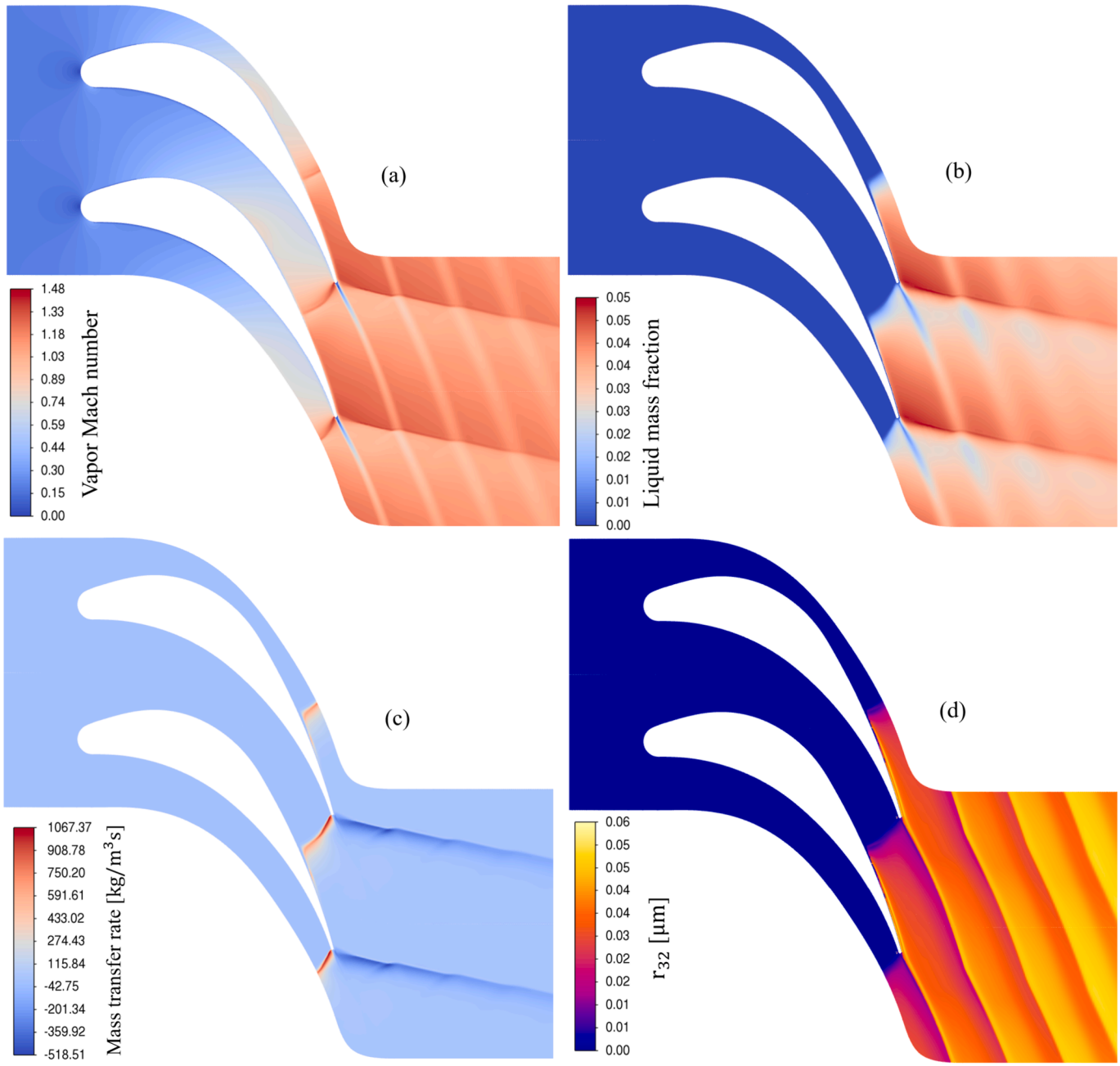

Fig. 17. Contours of Dykas turbine cascade for LP steam case 8: (a) vapor Mach number, (b) liquid mass fraction, (c) mass transfer rate and (d) r_{32}.

affects the increase of C_V. Therefore, nozzles with higher expansion rates would present a wider droplet size spectrum relative to r_{10}.

The normal and lognormal NDF evolutions along the nozzle axis are compared with the QMOM normalized weights in Figs. 14, 15 and 16 for cases 1, 3 and 6, respectively. In order to facilitate a meaningful comparison, the NDFs are scaled to unity ($\hat{f}_\eta$). As the C_V increases along the supersonic wet expansion, the weight related to the lowest radius obtained from QMOM increases as the radius decreases, and the weight corresponding to the second-highest radius decreases as the radius increases. Coherently, the NDFs become wider, with the normal NDF capturing the weights both at the beginning of the condensation region and farther downstream into the nozzle very well. On the other hand, the lognormal NDF is not an appropriate shape for capturing the weights distributions at higher C_V.

4.3. Turbine cascade analysis

The turbine cascade of Dykas [55] has been investigated numerically to study the effects of polydispersed methods in this geometry for both steam and CO_2. The contours of vapor Mach number, liquid mass fraction, mass transfer rate and Sauter radius are shown in Figs. 17 and 18 for LP steam (case 8) and CO_2 (case 10), respectively. The results are shown only for the normal NDF, which has achieved the best overall agreement with the experiments in nozzle flows. The plotted quantities remain almost unaffected between different methods, except for r_{32}, whose variations will be discussed later. The stator cascade is simulated with the same expansion ratio for both fluids, resulting in similar Mach number distributions and shock wave structures. The condensation and aerodynamic shock waves, experimentally identified using the Schlieren visualization method by Dykas et al. in [56], can be observed in the Mach number contours near the trailing edge of the blade. The external

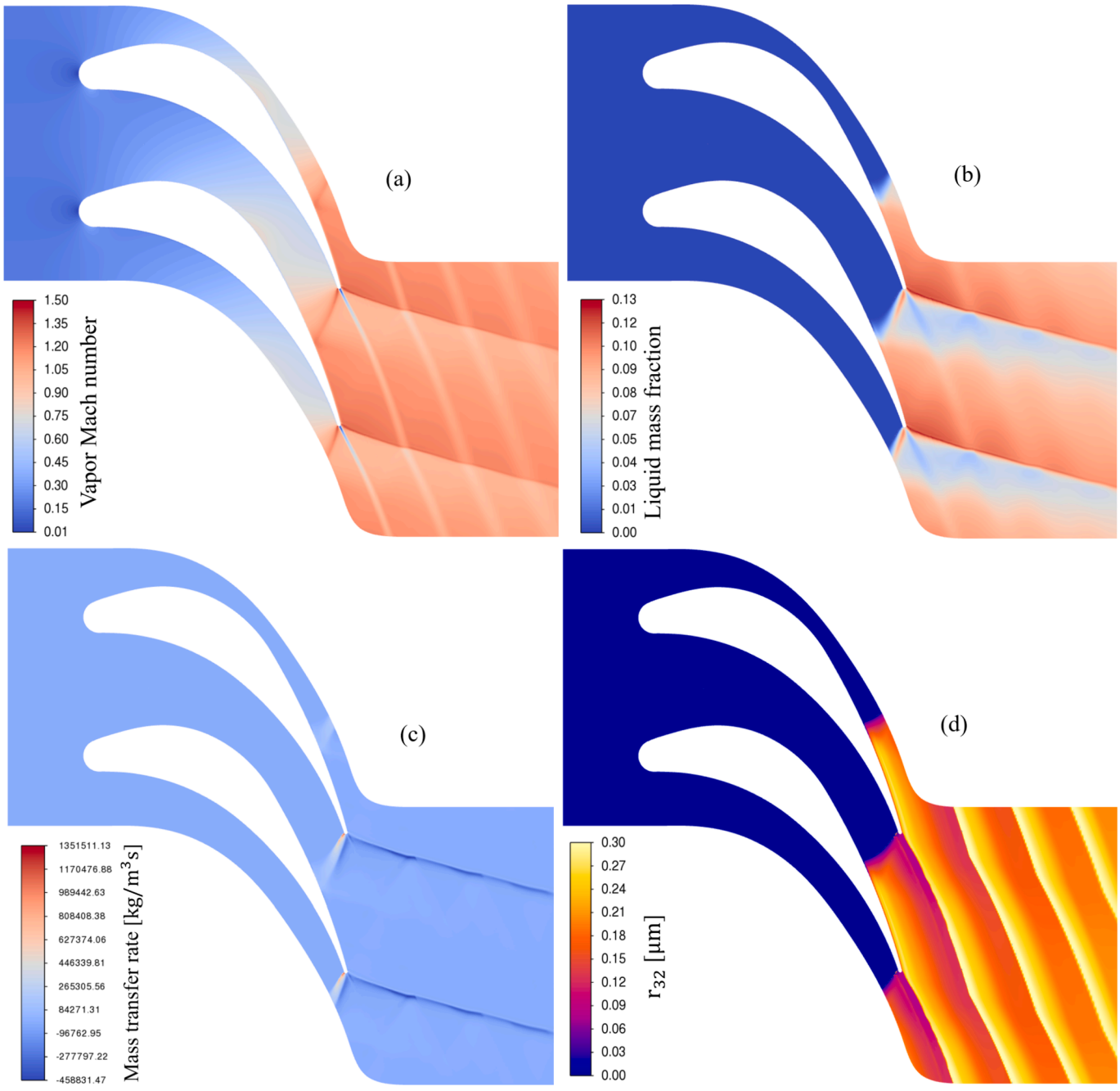

Fig. 18. Contours of Dykas turbine cascade for CO_2 case 10: (a) vapor Mach number, (b) liquid mass fraction, (c) mass transfer rate and (d) r_{32}.

and internal fishtail shocks at the trailing edge, reflected on the suction side, are well visible. The condensation onset occurs almost in the same spot of the oblique shock wave, making the pressure rise related to the condensation latent heat release indistinguishable. The internal fishtail shock wave impacts on the blade suction side for CO_2 with a larger angle than that observed in steam, and its reflection is better visible by the Mach number contours. The CO_2 inlet conditions have been selected in such a way that the nucleating region is in the same spot as the steam case. Nevertheless, the wetness fraction obtained for CO_2 is larger than that in steam, since the saturation curve is crossed near the critical point for CO_2. The mass transfer rates computed for CO_2 are three orders of magnitude larger than those for the steam case. Besides the larger wetness fraction, this huge difference is due to the very different vapor densities of the fluids in the corresponding thermodynamic regions.

The large mass transfer rate computed in the blade channel indicates the nucleating region, where the sudden formation of liquid droplets takes place in the supersaturated vapor. In correspondence of the external fishtail shock wave generated at the trailing edge, one main region with a negative mass transfer rates can be identified, indicating that the liquid droplets are partially evaporating. The Sauter radius sizes are larger for the CO_2 flow by approximately a factor of 5. Moreover, the larger droplets are found in correspondence with the flow close to the blade suction side for both cases.

The mass-weighted average of the Sauter radius and the coefficient of variation calculated at the outlet boundary for each case are reported in Figs. 19 and 20, respectively. QMOM predicts the lowest values of r_{32} for all cases, while the normal and lognormal NDF predict larger droplet sizes than the monodispersed model for CO_2 flows. For higher expansion ratios, higher values of the expansion rate are achieved in the blade channel, allowing deeper penetration into the metastable region and

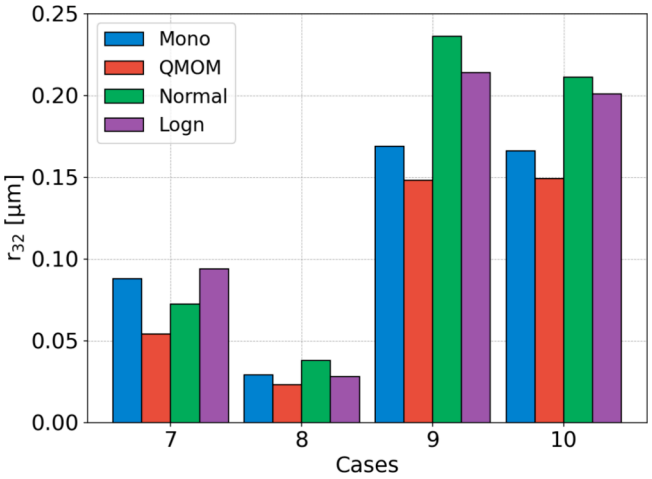

Fig. 19. Mass-weighted average r_{32} at the outlet for turbine cascade cases.

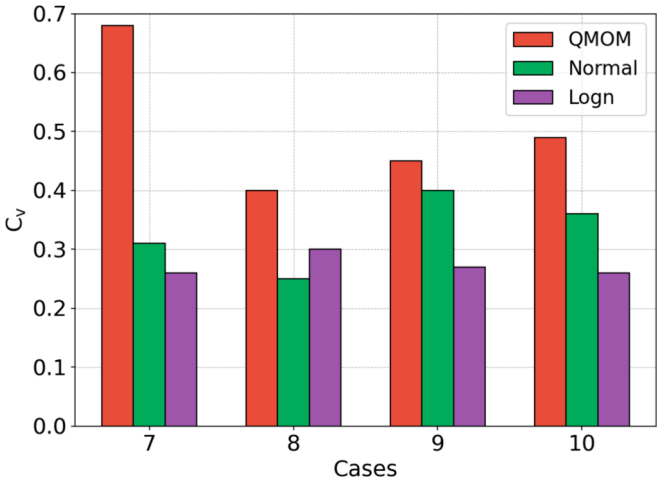

Fig. 20. Mass-weighted average C_V at the outlet for turbine cascade cases.

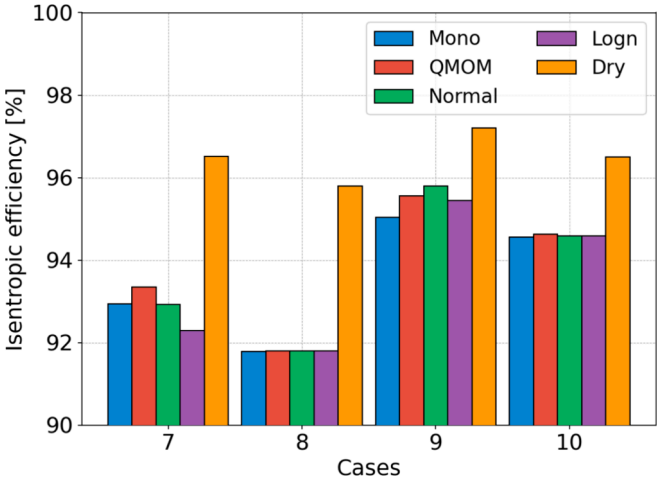

Fig. 21. Isentropic efficiency for turbine cascade cases.

leading to higher values of supersaturation and, consequently, higher nucleation rates. This phenomenon results in lower values of r_{32} obtained at higher speeds, especially for steam when moving from case 7 to case 8. Larger C_V values are predicted by QMOM compared to other

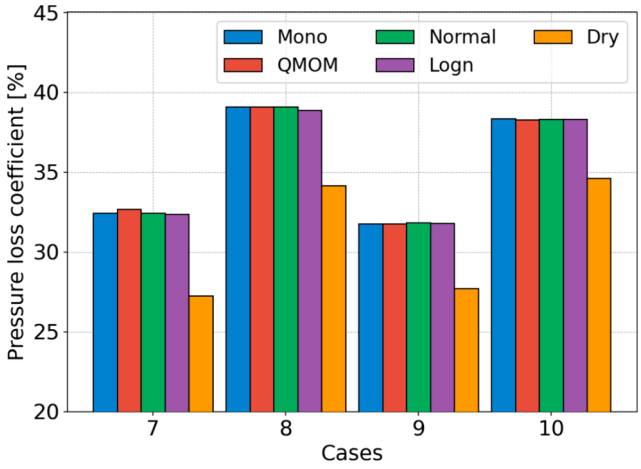

Fig. 22. Pressure loss coefficient for turbine cascade cases.

methods, indicating that the NDF distribution is wider in these simulations where the smallest droplet sizes are calculated.

The performance of the turbine blade cascade is evaluated by calculating its isentropic efficiency, defined as the ratio between the actual enthalpy drop and the ideal isentropic one, as shown in Eq. (42), and pressure loss coefficient, as defined in Eq. (43).

$$\eta_{is} = \frac{h_{0,in} - h_{out}}{h_{0,in} - h_{out,is}} \tag{42}$$

$$Y = \frac{p_{0,in} - p_{0,out}}{p_{0,in} - p_{out}}. \tag{43}$$

For the nucleating cases, h_{out} and $h_{out,is}$ were calculated assuming that the phases are in equilibrium at the outlet section. Additionally, to quantify the effects of the condensed droplets on these quantities, numerical simulations of dry flows have also been conducted for both steam and CO_2. The results obtained from CFD simulations are represented in Figs. 21 and 22 for the isentropic efficiency and the pressure loss coefficient, respectively.

Fig. 21 indicates that the isentropic efficiency for wet cases is impacted by the choice of the polydispersed model, particularly for lower expansion ratios (cases 7 and 9). For instance, in case 7, the QMOM predicts an efficiency of 93.34 %, while the lognormal NDF predicts a value of 92.29 %, which is a significant deviation for the performance of the machine. These differences become negligible at higher expansion ratios (cases 8 and 10), where a maximum difference of 0.08 % in efficiency is observed in case 10 between the monodispersed model and QMOM. The isentropic efficiencies for CO_2 cases are higher than those of steam cases. Considering the efficiencies calculated with the normal NDF, they increase from 92.93 % to 95.79 % between cases 7 and 9 (+2.86 %) and from 91.79 % to 94.59 % between cases 8 and 10 (+2.80 %). The predicted efficiency loss due to condensation, calculated as the difference between the efficiency of the dry case and that of the wet case, varies for different NDFs between 3.17 % and 4.22 % in steam and between 1.42 % and 2.18 % in CO_2. Hence, the condensation losses are much smaller in CO_2, even though the wetness fraction of the CO_2 flows is more than double that found in wet steam. One possible explanation for this outcome is that the thermodynamic and transport properties of liquid droplets do not differ much from the vapor properties for operating conditions near the critical point, as instead happens for condensing LP steam. Thus, the limited property variations of the mixture flow do not seem to significantly affect the efficiency of the turbine cascade.

Unlike the isentropic efficiency, the pressure loss coefficient, depicted in Fig. 22, is mostly dependent on the expansion ratio rather than the working fluid. Moreover, it does not vary much between the various

NDFs, with a maximum difference of 0.31 % between QMOM and the lognormal NDF in case 7. As observed with isentropic efficiency, droplet condensation worsens the performance of the blade cascade by increasing the pressure loss coefficient by 4.70–5.42 % for steam and by 3.65–4.11 % for CO_2. The pressure loss coefficient is primarily influenced by the overall flow dynamics around the turbine blades, including turbulence, separation, and wake formation. These phenomena are largely governed by the bulk properties of the flow, which are directly affected by phase change, rather than the detailed droplet characteristics. However, different droplet size distributions lead to varying interphase heat and mass transfers, which affect the thermodynamic path of the fluid expanding through the turbine, thereby having a major impact on the isentropic efficiency.

5. Conclusions

This paper presents a numerical model for simulating non-equilibrium condensing real gas flows with polydispersed droplet models. Results obtained with QMOM, and discrete methods based on normal and lognormal distributions are compared with experiments. Our study highlights the importance of accounting for polydispersed droplet sizes in condensing steam flows, achieving higher accuracy over monodispersed models in terms of pressure and Sauter radius distributions. Similar trends are also observed in high-pressure CO_2 flows, but the lack of droplet size measurements does not allow us to make definitive statements about the accuracy of the models.

The main conclusions of this paper are as follows:

- The QMOM and normal NDF better capture the pressure and Sauter radius distributions in converging–diverging nozzle geometries compared to the lognormal NDF. Moreover, the normal NDF closely matches the QMOM behavior, in contrast with the lognormal NDF, which exhibits issues in capturing the droplet size spectrum at higher values of the variation coefficient.
- The nozzle expansion rate significantly impacts the droplet size distributions, with higher expansion rates inducing larger dispersion of droplet sizes.
- Simulating steam and CO_2 condensing flows in a turbine cascade using polydispersed methods shows that QMOM predicts smaller values of the Sauter radius than normal and lognormal NDFs. Downstream of the blade cascade, QMOM also predicts higher variation coefficients, indicating a larger dispersion of droplet sizes.
- The isentropic efficiencies of the turbine blade cascade calculated for steam and CO_2 flows are affected by the choice of the polydispersed model at low expansion ratios, with variations in efficiency up to 1.05 %.
- The condensation losses through the turbine blade cascade are much smaller for CO_2 (1.42–1.91 %) than for steam (3.58–4.01 %), leading to higher isentropic efficiencies for CO_2 (94.59–95.79 %) compared to those obtained with steam (91.79–92.93 %)

This study offers crucial insights into the numerical modeling of polydispersed droplet sizes in condensing real gas flows and provides a valuable tool for simulating these flows with a commercial CFD solver. In future work, the model can be extended to simulate different geometries beyond nozzles and turbine blade cascades, such as CO_2 supersonic separators or ejectors, thereby improving their design and performance.

Declaration of competing interest

The authors declare that they have no known competing financial interests or personal relationships that could have appeared to influence the work reported in this paper.

Data availability

Data will be made available on request.

Acknowledgements

The authors gratefully acknowledge the financial support of the Doctoral School of Lappeenranta-Lahti University of Technology LUT.

References

[1] R. Allam, S. Martin, B. Forrest, J. Fetvedt, X. Lu, D. Freed, G.W. Brown, T. Sasaki, M. Itoh, J. Manning, Demonstration of the Allam cycle: an update on the development status of a high efficiency supercritical carbon dioxide power process employing full carbon capture, Energy Proc. 114 (2017) 5948–5966.
[2] F. Crespi, D. Sánchez, J.M. Rodríguez, G. Gavagnin, A thermo-economic methodology to select sCO2 power cycles for CSP applications, Renew. Energy 147 (3) (2020) 2905–2912.
[3] V. Dostal, P. Hejzlar, M.J. Driscoll, High-performance supercritical carbon dioxide cycle for next-generation nuclear reactors, Nucl. Technol. 154 (3) (2006) 265–282.
[4] A. Uusitalo, A. Ameli, T. Turunen-Saaresti, Thermodynamic and turbomachinery design analysis of supercritical Brayton cycles for exhaust gas heat recovery, Energy 167 (2019) 60–79.
[5] B.T. Austin, K. Sumathy, Transcritical carbon dioxide heat pump systems: A review, Renew. Sustain. Energy Rev. 15 (8) (2011) 4013–4029.
[6] A. Ameli, T. Turunen-Saaresti, J. Backman, Numerical Investigation of the Flow Behavior Inside a Supercritical CO2 Centrifugal Compressor, ASME. J. Eng. Gas Turbines Power 140 (12) (2018) 122604.
[7] N.D. Baltadjiev, C. Lettieri, Z.S. Spakovszky, An investigation of real gas effects in supercritical CO2 centrifugal compressors, ASME. J. Turbomach. 137 (9) (2015) 091003.
[8] G. Zhang, Y. Li, Z. Jin, S. Dykas, X. Cai, A novel carbon dioxide capture technology (CCT) based on non-equilibrium condensation characteristics: Numerical modelling, nozzle design and structure optimization, Energy 286 (2024) 129603.
[9] W. Jiang, J. Bian, A. Wu, S. Gao, P. Yin, D. Hou, Investigation of supersonic separation mechanism of CO2 in natural gas applying the Discrete Particle Method, Chem. Eng. Process. - Process Intesif. 123 (2018) 272–279.
[10] H. Ding, Y. Zhang, C. Sun, Y. Yang, C. Wen, Numerical simulation of supersonic condensation flows using Eulerian-Lagrangian and Eulerian wall film models, Energy 258 (2022) 124833.
[11] G. Zhang, Y. Yang, J. Chen, Z. Jin, M. Majkut, K. Smołka, S. Dykas, Effect of relative humidity on the nozzle performance in non-equilibrium condensing flows for improving the compressed air energy storage technology, Energy 280 (2023) 128240.
[12] G. Zhang, Y. Yang, J. Chen, Z. Jin, S. Dykas, Numerical study of heterogeneous condensation in the de Laval nozzle to guide the compressor performance optimization in a compressed air energy storage system, Appl. Energy 356 (2024) 122361.
[13] A.M. Dolatabadi, H.R. Mottahedi, M.A.F. Aliabadi, M.S. Pour, C. Wen, M. Akrami, Evaluating and optimizing of steam ejector performance considering heterogeneous condensation using Machine learning framework, Energy 132240 (2024).
[14] A.M. Dolatabadi, M.A.F. Aliabadi, Evaluating sustainability power plant efficiency: Unveiling the impact of power plant load ratio on holding steam ejector performance, Energy 305 (2024) 132315.
[15] S.M.A. Noori Rahim Abadi, R. Kouhikamali, K. Atashkari. Two-fluid model for simulation of supersonic flow of wet steam within high-pressure nozzles. International Journal of Thermal Sciences 96, 173-182 (2015).
[16] A.M. Dolatabadi, M.J. Eghbali, Ț. Florin-Emilian, E. Mohamadpour, R. Amini, Performance evaluation of condensing flow behavior considering magneto hydrodynamics field effects, Appl. Therm. Eng. 219 (B) (2023) 119472.
[17] G. Petruccelli, A. Grönman, A.T. Turunen-Saaresti, A novel numerical approach for simulating low-pressure and high-pressure non-equilibrium condensation in real gases, Int. J. Multiph. Flow 171 (2024) 104700.
[18] T. Furusawa, H. Miyazawa, S. Moriguchi, S. Yamamoto. Numerical Method for Simulating High Pressure CO2 Flows With Nonequilibrium Condensation. Proceedings of the ASME Turbo Expo 2018: Turbomachinery Technical Conference and Exposition. Volume 9: Oil and Gas Applications; Supercritical CO2 Power Cycles; Wind Energy. Oslo, Norway. V009T38A012. ASME.
[19] G. Zhang, X. Wang, Z. Jin, S. Dykas, K. Smołka, Numerical study of the loss and power prediction based on a modified non-equilibrium condensation model in a 200 MW industrial-scale steam turbine under different operation conditions, Energy 275 (2023) 127530.
[20] A.M. Dolatabadi, J. Moslehi, M.S. Pour, S.S.M. Ajarostaghi, S. Poncet, M. Arıcı, Modified model of reduction condensing losses strategy into the wet steam flow considering efficient energy of steam turbine based on injection of nano-droplets, Energy 242 (2022) 122951.
[21] Y. Patel, G. Patel, T. Turunen-Saaresti, Influence of turbulence modelling on non-equilibrium condensing flows in nozzle and turbine cascade, Int. J. Heat Mass Transf. 88 (2015) 165–180.
[22] F. Giacomelli, F. Mazzelli, A. Milazzo, A novel CFD approach for the computation of R744 flashing nozzles in compressible and metastable conditions, Energy 162 (2018) 1092–1105.

[23] J. Smolka, Z. Bulinski, A. Fic, A.J. Nowak, K. Banasiak, A. Hafner, A computational model of a transcritical R744 ejector based on a homogeneous real fluid approach, App. Math. Model. 37 (3) (2013) 1208–1224.
[24] A. Romei, G. Persico, Computational fluid-dynamic modelling of two-phase compressible flows of carbon dioxide in supercritical conditions, Appl. Therm. Eng. 190 (2021) 116816.
[25] A.J. White, J.B. Young. Time-marching method for the prediction of two-dimensional, unsteady flows of condensing steam. J. Propul. Power 9 (4), (1993).
[26] A.G. Gerber, Two-phase Eulerian/Lagrangian model for nucleating steam flow, J. Fluids Eng. 124 (2002) 465–475.
[27] A.G. Gerber, M.J. Kermani, A pressure based Eulerian-Eulerian multi-phase model for non-equilibrium condensation in transonic steam flow, Int. J. Heat Mass Transf. 47 (10–11) (2004) 2217–2231.
[28] A.J. White, A comparison of modelling methods for polydispersed wet-steam flow, Int. J. Numer. Meth. Eng. 57 (6) (2003) 819–834.
[29] A.J. White, M.J. Hounslow, Modelling droplet size distributions in polydispersed wet-steam flows, Int. J. Heat Mass Transf. 43 (11) (2000) 1873–1884.
[30] R. McGraw, Description of aerosol dynamics by the quadrature method of moments, Aerosol. Sci. Tech. 27 (2) (1997) 255–265.
[31] A.G. Gerber, A. Mousavi, Representing polydispersed droplet behavior in nucleating steam flow, J. Fluids Eng. 129 (11) (2007) 1404–1414.
[32] A. Afzalifar, T. Turunen-Saaresti, A. Grönman, Comparison of Moment-Based Methods for Representing Droplet Size Distributions in Supersonic Nucleating Flows of Steam, ASME. J. Fluids Eng. 140 (2) (2018) 021301.
[33] H. Ding, Y. Tian, C. Wen, C. Wang, C. Sun, Polydispersed droplet spectrum and exergy analysis in wet steam flows using method of moments, Appl. Therm. Eng. 182 (2021) 116148.
[34] M.J. Hounslow, R.L. Ryall, V.R. Marshall, A discretized population balance for nucleation, growth, and aggregation, AIChE J 34 (11) (1988) 1821–1832.
[35] J.D. Lister, D.J. Smit, M.J. Hounslow, Adjustable discretized population balance for growth and aggregation, AIChE J 41 (3) (1995) 591–603.
[36] S. Park, K. Lee, M. Shimada, K. Okuyama, Alternative analytical solution to condensational growth of polydisperse aerosols in the continuum regime, J. Aerosol Sci 32 (2) (2001) 187–197.
[37] W. Wroblewski, S. Dykas, Two-fluid model with droplet size distribution for condensing steam flows, Energy 106 (2016) 112–120.
[38] F.R. Menter, Two-equation eddy-viscosity turbulence models for engineering applications, AIAA J. 32 (8) (1994) 1598–1605.
[39] D.L. Marchisio, J.T. Pikturna, R.O. Fox, R.D. Vigil, A.A. Barresi, Quadrature Method of Moments for Population-Balance Equations, AIChE J. 49 (5) (2003) 1266–1276.
[40] R. Span, W. Wagner, A new equation of state for carbon dioxide covering the fluid region from the triple-point temperature to 1100 K at pressures up to 800 MPa, J. Phys. Chem. Ref. Data 25 (6) (1996) 1509–1596.
[41] W. Wagner, A. Pruß, The IAPWS Formulation 1995 for the Thermodynamic Properties of Ordinary Water Substance for General and Scientific Use, J. Phys. Chem. Ref. Data 31 (2) (2002) 387–535.
[42] E.W. Lemmon, I.H. Bell, M.L. Huber, M.O. McLinden, NIST Standard Reference Database 23: Reference Fluid Thermodynamic and Transport Properties-REFPROP, Version 10.0, National Institute of Standards and Technology, Standard Reference Data Program, Gaithersburg, 2018.
[43] A. Afzalifar, T. Turunen-Saaresti, A. Grönman, Nonrealizability Problem with Quadrature Method of Moments in Wet-Steam Flows and Solution Techniques, J. Eng. Gas Turbines Power 139 (1) (2017) 012602.
[44] J.C. Wheeler, Modified moments and Gaussian quadratures, Rocky Mountain Journal of Mathematics 4 (1974) 287–296.
[45] D.L. Marchisio, R.O. Fox, Computational Models for Polydisperse Particulate and Multiphase Systems, Cambridge University Press, Cambridge, UK, 2013.
[46] S.H. Bryngelson, T. Colonius, R.O. Fox, QBMMlib: A library of quadrature-based moment methods, SoftwareX 12 (2020) 100615.
[47] MathWorks Inc., NIST. JAMA-A Java Matrix Package. http://math.nist.gov/javanumerics/jama/.
[48] H. Bowdler, R.S. Martin, C. Reinsch, J.H. Wilkinson. The QR and QL Algorithms for Symmetric Matrices. In: Bauer, F.L., Householder, A.S., Olver, F.W.J., Rutishauser, H., Samelson, K., Stiefel, E. (eds) Handbook for Automatic Computation. Die Grundlehren der mathematischen Wissenschaften, vol 186. Springer, Berlin, Heidelberg (1971).
[49] R. Becker, W. Döring, Kinetische behandlung der keimbildung in übersättigten dämpfen, Annalen der Physik 416 (8) (1935) 719–752.
[50] W.G. Courtney, Remarks on homogeneous condensation, J. Chem. Phys. 35 (1961) 2249–2250.
[51] G. Gyarmathy, Zur Wachstumsgeschwindigkeit kleiner Flüssigkeitstropfen in einer übersättigten Atmosphäre, Journal of Applied Mathematics and Physics (ZAMP) 14 (1963) 280–293.
[52] M.E. Maqueo Martinez, S. Schippling, M. Schatz, D.M. Vogt. New supersonic nozzle test-rig used to generate condensing flow test data according to Barschdorff. Proceedings of 15th European Conference on Turbomachinery Fluid dynamics & Thermodynamics ETC15, Budapest, Hungary (2023).
[53] G. Gyarmathy, Nucleation of steam in high-pressure nozzle experiments, Proceedings of the Institution of Mechanical Engineers, Part a: Journal of Power and Energy 219 (6) (2005) 511–521.
[54] C. Lettieri, D. Paxson, Z. Spakovszky, P. Bryanston-Cross, Characterization of Nonequilibrium Condensation of Supercritical Carbon Dioxide in a de Laval Nozzle, ASME. J. Eng. Gas Turbines Power 140 (4) (2018) 041701.
[55] S. Dykas, M. Majkut, M. Strozik, K. Smołkaj, Experimental study of condensing steam flow in nozzles and linear blade cascade, Int. J. Heat Mass Transf. 80 (2015) 50–57.
[56] S. Dykas S, M. Majkut, K. Smołka, M. Strozik. Analysis of the steam condensing flow in a linear blade cascade. Proc. Inst. Mech. Eng., Part A: J. Power Energy 232 (5), 501-514 (2018).